Article

B-cell-specific checkpoint molecules that regulate anti-tumour immunity

https://doi.org/10.1038/s41586-023-06231-0

Received: 2 November 2021

Accepted: 17 May 2023

Published online: 21 June 2023

Check for updates

Lloyd Bod[1,2,3,11], Yoon-Chul Kye[1,2,3], Jingwen Shi[1,2,12], Elena Torlai Triglia[2], Alexandra Schnell[1,2,3], Johannes Fessler[1,13], Stephen M. Ostrowski[4], Max Y. Von-Franque[4], Juhi R. Kuchroo[1,5], Rocky M. Barilla[1,3], Sarah Zaghouani[1], Elena Christian[2], Toni Marie Delorey[2], Kanishka Mohib[6], Sheng Xiao[1], Nadine Slingerland[1,2], Christopher J. Giuliano[2], Orr Ashenberg[2], Zhaorong Li[7], David M. Rothstein[6], David E. Fisher[4], Orit Rozenblatt-Rosen[2,8], Arlene H. Sharpe[1,5], Francisco J. Quintana[2,8], Lionel Apetoh[1,9,10], Aviv Regev[2,8,14] ✉ & Vijay K. Kuchroo[1,2,3] ✉

The role of B cells in anti-tumour immunity is still debated and, accordingly, immunotherapies have focused on targeting T and natural killer cells to inhibit tumour growth[1,2]. Here, using high-throughput flow cytometry as well as bulk and single-cell RNA-sequencing and B-cell-receptor-sequencing analysis of B cells temporally during B16F10 melanoma growth, we identified a subset of B cells that expands specifically in the draining lymph node over time in tumour-bearing mice. The expanding B cell subset expresses the cell surface molecule T cell immunoglobulin and mucin domain 1 (TIM-1, encoded by *Havcr1*) and a unique transcriptional signature, including multiple co-inhibitory molecules such as PD-1, TIM-3, TIGIT and LAG-3. Although conditional deletion of these co-inhibitory molecules on B cells had little or no effect on tumour burden, selective deletion of *Havcr1* in B cells both substantially inhibited tumour growth and enhanced effector T cell responses. Loss of TIM-1 enhanced the type 1 interferon response in B cells, which augmented B cell activation and increased antigen presentation and co-stimulation, resulting in increased expansion of tumour-specific effector T cells. Our results demonstrate that manipulation of TIM-1-expressing B cells enables engagement of the second arm of adaptive immunity to promote anti-tumour immunity and inhibit tumour growth.

B cells have key roles in both innate and adaptive immunity. Distinct specialized B cell subsets engage a range of responses from antigen presentation to antibody production and B cells are one of the most abundant cell types of tumour-infiltrating leukocytes (TILs)[3], especially in melanoma[4,5]. However, the role of B cells in anti-tumour immunity remains unclear. Here we examine the B cell repertoire at the single-cell resolution from tumour-infiltrating B cells and tumour-draining lymph nodes (dLNs) and identify and characterize a subset of B cells expressing the checkpoint molecule TIM-1. We find that targeting TIM-1 enables engagement of this B cell subset, with subsequent enhancement of anti-tumour $CD8^+$ and $CD4^+$ T cell responses and inhibition of tumour cell growth, with implications for approaches to cancer therapy.

Distinct B cell infiltrates in B16F10 TME

To understand the role of B cell subsets in regulating immune responses to tumours, we characterized B cells from tumours, dLNs and non-draining LNs (ndLNs) in the B16F10 melanoma mouse model. We confirmed that B cells infiltrate the tumour and are increased in frequency within the dLN compared with in the ndLN (Extended Data Fig. 1a). Depletion of B cells globally using anti-CD20 monoclonal antibodies significantly enhanced melanoma tumour growth; however, abrogating plasma cell generation (using $Cd19^{cre/+}Prdm1^{fl/fl}$ mice) did not affect the tumour burden (Extended Data Fig. 1b,c). Tumour-infiltrating B cells had distinct expression profiles on the basis of bulk RNA-sequencing (RNA-seq) analysis compared with B cells from lymphoid tissues, reflecting the induction of proliferative and migratory pathways associated with B cell activation (Extended Data Fig. 1d–g). Moreover, tumour-infiltrating B cells were predominantly follicular B cells of the B2 lineage with bimodal IgD expression (Extended Data Fig. 1h). Thus, although plasma cells seemed to be dispensable, total B cells produced an anti-tumour effect and displayed a distinct phenotype after infiltration in B16F10 tumours, prompting a deeper analysis.

[1]Evergrande Center for Immunologic Diseases, Harvard Medical School and Brigham and Women's Hospital, Boston, MA, USA. [2]Klarman Cell Observatory, Broad Institute of MIT and Harvard, Cambridge, MA, USA. [3]Gene Lay Institute of Immunology and Inflammation, Brigham and Women's Hospital, Massachusetts General Hospital and Harvard Medical School, Boston, MA, USA. [4]Department of Dermatology, Massachusetts General Hospital, Boston, MA, USA. [5]Department of Microbiology and Immunobiology, Harvard Medical School, Boston, MA, USA. [6]Thomas E. Starzl Transplantation Institute, University of Pittsburgh School of Medicine, Pittsburgh, PA, USA. [7]Ann Romney Center for Neurologic Diseases, Brigham and Women's Hospital, Harvard Medical School, Boston, MA, USA. [8]Howard Hughes Medical Institute, Department of Biology and Koch Institute of Integrative Cancer Research, Massachusetts Institute of Technology, Cambridge, MA, USA. [9]INSERM, Tours, France. [10]Faculté de Médecine, Université de Tours, Tours, France. [11]Present address: Massachusetts General Hospital Cancer Center, Department of Medicine, Massachusetts General Hospital, Harvard Medical School, Boston, MA, USA. [12]Present address: BeiGene, Beijing, China. [13]Present address: Division of Immunology and Pathophysiology, Medical University of Graz, Graz, Austria. [14]Present address: Genentech, San Francisco, CA, USA. ✉e-mail: aviv.regev.sc@gmail.com; vkuchroo@rics.bwh.harvard.edu

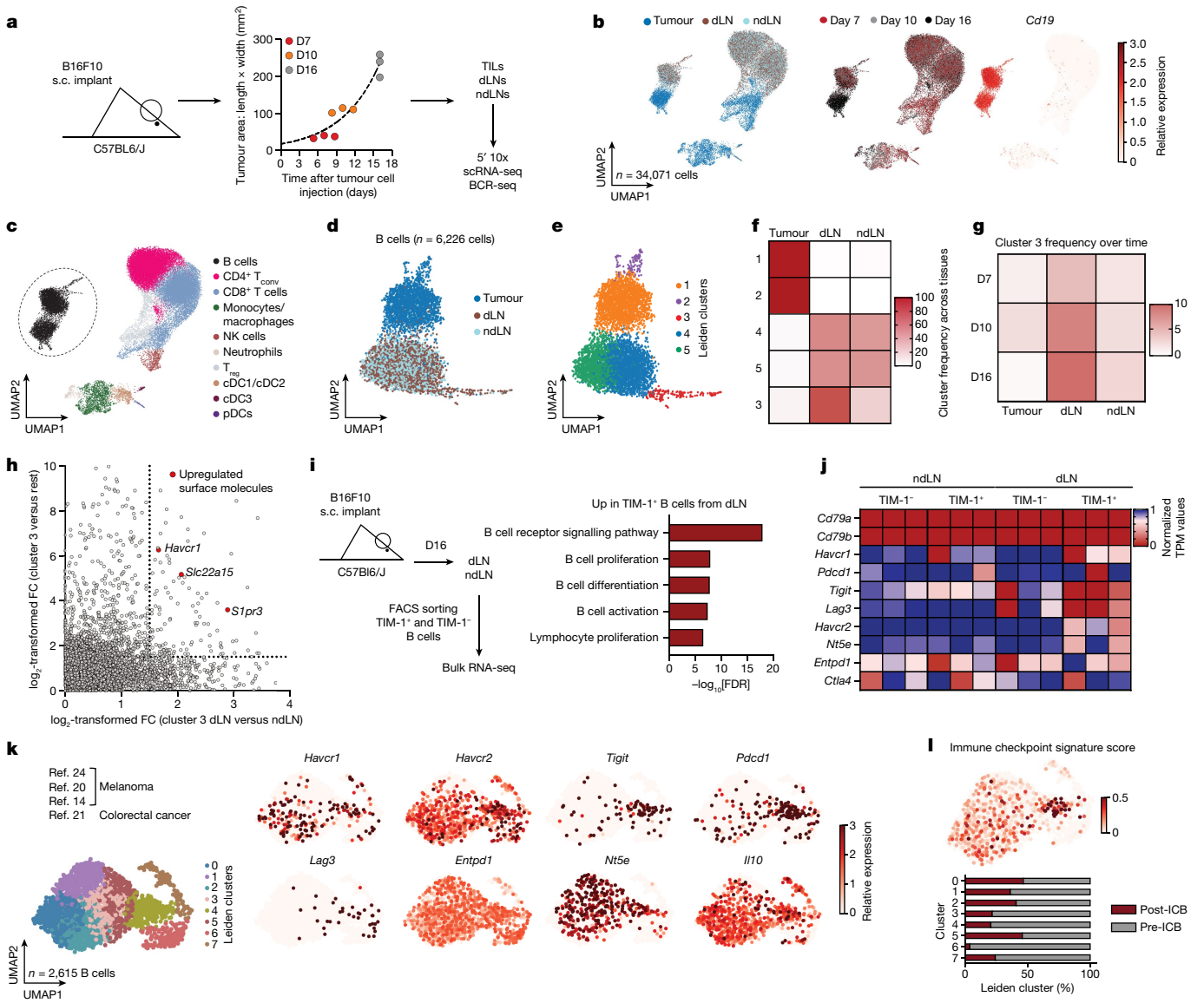

Fig. 1 | Characterization of B cells expressing TIM-1 and several checkpoint molecules in mouse melanoma and human tumours. a, Workflow for single-cell transcriptome profiling of 34,071 viable leukocytes from TME, dLN and ndLN samples. $n = 3$ mice per time point (days 7 (D7; early), 10 (intermediate) and 16 (late)). s.c., subcutaneous. **b**, Uniform manifold approximation and projection (UMAP) embedding of all cells sequenced with each colour representing tissues of origin (left), timepoint (centre) and expression of *Cd19* (right). **c**, UMAP visualization of the immune cell types. $CD4^+$ T_{conv}, conventional $CD4^+$ T cells; cDC1/2/3, type 1, 2 and 3 conventional dendritic cells; NK, natural killer. **d**,**e**, UMAP visualization of the 6,226 B cells (dots) collected from wild-type mice bearing B16F10 melanoma, depicting tissues of origin (**d**) or Leiden cell clusters (resolution 0.85) (**e**). **f**,**g**, The frequencies of cells from each cluster within the tissues of origin (**f**) or from cluster 3 over time and tissues of origin (**g**). **h**, The $\log_2$-transformed fold change (FC) in RNA levels between B cells derived from cluster 3 with the rest of the clusters and between the dLN and ndLN. **i**,**j**, Bulk RNA-seq analysis of TIM-1^+ and TIM-1^- B cells derived from dLNs and ndLNs of B16F10-bearing wild-type mice. $n = 3$. **i**, Pathway enrichment analysis of dLN-derived TIM-1^+ B cells. FACS, fluorescence-activated cell sorting; FDR, false-discovery rate. **j**, The expression pattern of a set of selected genes. **k**,**l**, UMAP plot of published scRNA-seq[14,20,21,24] data depicting 2,615 B cells (dots) isolated from human tumours, coloured by cell clusters (**k**, left), selected gene expression (**k**, right) and immune checkpoint signature score (**l**, top), and a stacked bar graph displaying the frequencies of B cells derived from responder and pre- and post-ICB samples among each Leiden cluster (**l**, bottom).

B16F10 tumour growth induces a specific B cell subset

To further decipher B cell heterogeneity, we performed 5′ single-cell RNA-seq (scRNA-seq) combined with VDJ/B cell receptor (BCR)-seq (scRNA/BCR-seq) analysis of $CD45^+$ cells in the tumour microenvironment (TME), dLN and ndLN at three different timepoints of B16F10 melanoma growth (Fig. 1a,b and Extended Data Fig. 2). The 34,071 high-quality cell profiles were grouped by respective lineages and tissue origin, and expressed known marker genes, which we used for their annotation (Fig. 1c and Extended Data Fig. 2c). We searched for B cell populations that were expanded over time or in the three compartments (tumour, dLN and ndLN) on the basis of either transcriptional states or BCR clones (Fig. 1d and Extended Data Fig. 2d–h). Although known B cell subset expression signatures and markers did not identify discrete B cell groups (except for germinal-centre-like B cells; Extended Data Fig. 2g), unsupervised graph clustering partitioned them into five distinct clusters (Fig. 1e and Extended Data Fig. 2h). The main separation was by tissue origin (Fig. 1f), with clusters 1 and 2 comprising tumour-infiltrating B cells with a highly activated or inflammatory phenotype (*Cd69*, *Cd86* or *Cxcr4* in cluster 1; *Cd274*, *Apoe* or *Hspa1a* in

cluster 2), clusters 4 and 5 consisting of both dLN and ndLN B cells with a naive-like profile (*Cr2*, *Cxcr5*, *Tnfrsf13c* in cluster 4; *Fcer2a*, *Tnfrsf13b* in cluster 5) and cluster 3 mainly comprising cells from the tumour dLN with proliferative and germinal-centre-like profiles (*Mki67*, *Aicda*). The frequency of dLN cells in cluster 3 B cells augmented over time as tumours increased in size, suggesting a specific induction of cluster 3 in response to melanoma growth (Fig. 1g), consistent with the expression of activation and germinal centre B cell signatures in these cells. Moreover, BCR-based clonal analysis (using Immcantation)[6] identified only a small fraction of cells expressing immunoglobulin heavy chain gamma (*IGHG*), and those cells were predominantly members of cluster 3 and were moderately clonally expanded within the dLN compartment (Extended Data Fig. 2d,e).

TIM-1 marks checkpoint-expressing B cells

We sought to isolate and purify the B cell subset that increases with tumour growth by identifying cell surface markers that are expressed on this B cell population. The dLN-derived expanded cluster 3 B cells expressed genes encoding specific cell surface markers, especially *Havcr1*, encoding TIM-1 (using COMET[7]; Fig. 1h and Extended Data Fig. 2f). In the B16F10 tumour model, TIM-1$^+$ B cells poorly infiltrated the tumour but were found in the lymphoid organs and increased preferentially within the dLN (Extended Data Fig. 3a), consistent with our RNA profiles. TIM-1 is a member of the TIM family, of which TIM-3 is the most characterized molecule in the context of autoimmunity and anti-tumour immunity[8]. TIM-1 is not well studied in the context of cancer but is expressed on a fraction (around 10%) of peripheral B cells and can promote tissue tolerance by binding to phosphatidylserine exposed on apoptotic cells[9–13].

Sorted TIM-1$^+$ and TIM-1$^-$ B cells from the dLN and ndLN of B16F10-bearing mice showed distinct transcriptional profiles on the basis of bulk RNA-seq and flow cytometry analysis (Fig. 1i,j and Extended Data Fig. 3b,c), clustering by TIM-1 expression and not tissue origin, with TIM-1$^+$ B cells from the dLN displaying a unique expression signature, enriched in B cell activation and proliferation genes (Fig. 1i and Extended Data Fig. 3b,c). These features of TIM-1$^+$ B cells were confirmed functionally in vitro, as TIM-1$^+$ B cells had increased proliferation and differentiation into plasma cells (Extended Data Fig. 3d).

However, scRNA-seq analysis of sorted TIM-1$^+$ and TIM-1$^-$ B cells from the dLN, ndLN and spleen showed that germinal-centre-like TIM-1$^+$ B cells consist of only around 25% of all TIM-1-expressing B cells (Extended Data Fig. 3e–g), indicating that TIM-1 is not simply a marker of germinal centres, or a unique B cell lineage. Instead, our data suggest that TIM-1 may be expressed on all B cells during B cell activation. Consistent with this model, TIM-1 is transiently induced across cell divisions on the cell surface of TIM-1$^-$ B cells after B cell activation in vitro with BCR and/or CD40 but not lipopolysaccharide (LPS), supporting that TIM-1 could be induced on all B cells after antigen-driven B cell activation (Extended Data Fig. 3h).

Notably, TIM-1$^+$ B cells from the dLN of B16F10 tumour-bearing mice also express higher levels of various co-inhibitory and immunoregulatory molecules that are expressed on T cells, including PD-1, TIGIT, LAG3, TIM-3, CD39, CD73 and IL-10 (Fig. 1j and Extended Data Fig. 4a,b). These molecules were preferentially induced on TIM-1$^+$ B cells compared with on TIM-1$^-$ B cells after treatment with anti-IgM or anti-CD40 antibodies or LPS stimulation in vitro (Extended Data Fig. 4c).

To study the relevance of TIM-1$^+$ B cells in human tumours, we reanalysed TILs from human tumours using publicly available datasets that we and others have previously generated with high sensitivity (Smart-seq2 protocol)[4,14–24]. While focusing on tumour-infiltrating B cells derived from immune checkpoint blockade (ICB)-naive samples, we identified a cluster of B cells (cluster 4) co-expressing TIM-1 and multiple co-inhibitory molecules (*HAVCR2*, *TIGIT*, *PDCD1*, *LAG3*) and *IL10*, comprising a distinct B cell subset and a signature that overlaps with human exhausted T cells[14] (Fig. 1k–l and Extended Data Fig. 4d,e). Notably, cells in cluster 4, which largely included TIM-1$^+$ B cells, were more frequent among B cells derived from ICB-naive patients and were decreased in TILs after checkpoint blockade therapy in human tumours (Fig. 1l and Extended Data Fig. 4f,g). We corroborated these findings by investigating additional human cancer datasets derived from breast, colorectal, ovarian and lung tumours in which we could identify a similar cluster of B cells expressing checkpoint receptors (IC$^+$) enriched in ICB-naive patient samples (Extended Data Fig. 4h–j). Clinically, high expression of *HAVCR1* correlated with poor overall survival in patients with lung, pancreatic and stomach adenocarcinomas, while being protective in the context of colorectal cancer (Extended Data Fig. 4k,l). Furthermore, except for a poor impact on survival for stomach cancer, a high score for the IC$^+$ B cell signature did not affect the clinical outcomes of the patients (Extended Data Fig. 4m). These data indicate that TIM-1 marks a subset of activated B cells expressing co-inhibitory molecules and IL-10 in both mouse and human tumours and their presence in human tumours seems to be inhibited after checkpoint blockade therapy.

Genetic deletion of TIM-1 in B cells limits tumour growth

As TIM-1$^+$ B cells expressed multiple known T cell checkpoint molecules, some previously reported in B cells[25–29], we investigated their B-cell-intrinsic roles in regulating anti-tumour immunity. Conditional deletion of the checkpoint molecules *Havcr2*, *Tigit*, *Pdcd1* (encoding PD-1) or *Lag3* in B cells had a modest impact or no effect on tumour growth (Fig. 2a–e). Only loss of TIGIT on B cells led to a modest but significant decrease in tumour growth. Although IL-10 has previously been associated with regulatory B cells[25,30] and shown to be a critical driver of B cell regulatory function[31], loss of B-cell-specific IL-10 had no effect on B16F10 growth, arguing against a functional role of IL-10-producing B cells in this melanoma model (Fig. 2f).

Conversely, conditional deletion of *Havcr1* on B cells substantially inhibited tumour growth in various B16F10 melanoma tumour models, as well as MC38 colon carcinoma or KP1.9 lung adenocarcinoma (Fig. 2g–i and Extended Data Fig. 5a–e), indicating that TIM-1 is not only a marker of checkpoint-receptor-expressing B cells, but that TIM-1 has a functional role in regulating tumour growth in vivo. Notably, although TIM-1 was initially described to be expressed on T cells, *Havcr1* conditional deletion using *Cd4^{cre}*, which deleted TIM-1 on all T cells, had no effect on tumour growth in mice implanted with B16F10 melanoma (Extended Data Fig. 5f,g), supporting a cell-intrinsic role of TIM-1 in B cell function. Together, these data demonstrate an important role of TIM-1 specifically expressed on B cells in regulating anti-tumour immune responses and tumour growth in vivo.

Therapeutic targeting of TIM-1 reduces tumour growth

To examine whether acute deletion of *Havcr1* also regulates tumour growth, we generated *hCD20.TamCre* × *Havcr1$^{fl/fl}$* (hereafter, *Havcr1^{iBKO}*) mice and treated the mice with tamoxifen to trigger acute Cre-mediated *Havcr1* deletion and observed inhibition of tumour growth similar to that with constitutive deletion of *Havcr1* in B cells (Extended Data Fig. 5h). Moreover, this indicates that deletion of TIM-1 on B cells using another Cre driver independent of *Cd19^{cre}* induces similar control of tumour growth.

Next, therapeutic administration of a commercially available high-affinity anti-TIM-1 antibody (3B3) also induced marked inhibition of B16F10 tumour growth (Extended Data Fig. 5i). This therapeutic effect required the presence of B cells, and of TIM-1 expression on B cells, such that the therapeutic effect of the anti-TIM-1 antibody was lost in μMT (lacking B cells) or *Havcr1^{BKO}* mice (Fig. 3a and Extended Data Fig. 5i,j). Notably, we found that anti-TIM-1 treatment had a therapeutic effect inhibiting tumour growth selectively in mice with intact MHCII

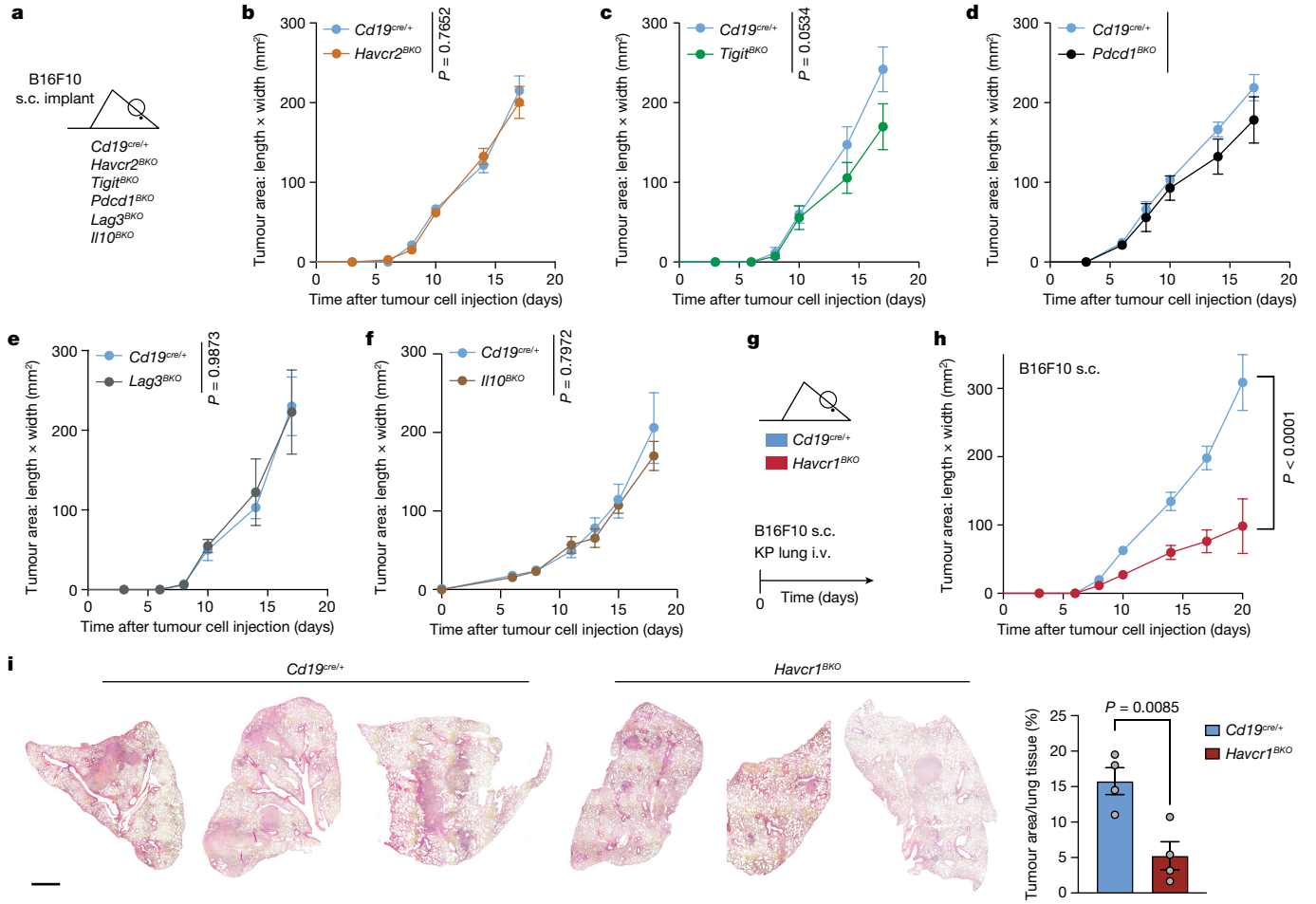

Fig. 2 | Screening of in vivo regulatory molecules reveals TIM-1 as a B cell immune checkpoint controlling tumour growth. a–**f**, Subcutaneous (s.c.) B16F10 melanoma growth in *Cd19*$^{cre/+}$ ($n = 5$), *Havcr2*^{BKO} ($n = 5$) (**b**), *Tigit*^{BKO} ($n = 6$) (**c**), *Pdcd1*^{BKO} ($n = 4$) (**d**), *Lag3*^{BKO} ($n = 4$) (**e**) and *Il10*^{BKO} ($n = 4$ controls versus $n = 4$ *Il10*^{BKO}) (**f**) mice. **a**, Experimental schematic. **g**–**i**, Schematic (**g**), quantification (**h**) and imaging (**i**) of tumour growth in *Cd19*$^{cre/+}$ and *Havcr1*^{BKO} mice implanted s.c. with B16F10 ($n = 6$ control versus $n = 9$ *Havcr1*^{BKO}) or intravenously (i.v.) injected with KP1.9 cells ($n = 4$ mice per group). Tumour burden was assessed by histological analysis of lung tissue collected 4 weeks after injection. Data are mean ± s.e.m. and pooled from two to three independent experiments. Statistical analysis was performed using repeated-measures two-way analysis of variance (ANOVA) (**b**–**f** and **h**) and two-tailed Student's *t*-tests (**i**). Scale bar, 1 mm (**i**).

expression on the B cell surface (Extended Data Fig. 5k). Whereas 3B3 has previously been reported to be an agonistic antibody based on activating T cell effector functions, in B cells, the effects of the 3B3 antibody are very similar to what we observed after the genetic loss of TIM-1 on B cells. Whether this is due to differential effects of TIM-1 on T cells versus B cells needs to be further characterized; nonetheless, the therapeutic effects of anti-TIM-1 antibodies on tumour growth are unequivocal. As TIM-1 expression on T cells has no effect on tumour growth, in vivo effects of anti-TIM-1 antibodies appear to be entirely dependent on the expression of TIM-1 on B cells. Moreover, we performed anti-TIM-1 treatment experiments using the spontaneous melanoma model: *Tyr-cre*^{ERT2}*Braf*$^{CA/WT}$*Pten*$^{lox/lox}$ (hereafter *Braf-Pten*) mice carrying a tamoxifen-inducible Cre-recombinase under the control of the tyrosinase promoter. This model enables melanocyte lineage-specific induction of a BRAF(V600E) mutation and deletion of *Pten*, inducing spontaneous formation of melanoma and replicating many of the features of human melanoma. Notably, treatment with anti-TIM-1 (clone 3B3) significantly reduced melanoma genesis and proximal metastatic dissemination (Fig. 3b,c). Finally, combined PD-1 blockade (as a T-cell-relevant target) together with anti-TIM-1 antibody treatment had an additive effect, consistent with an impact on two different compartments, resulting in more rapid and consistent growth control and prolonged survival in B16F10-bearing mice compared with either treatment alone (Fig. 3d and Extended Data Fig. 5l). Monotherapy with anti-TIM-1 antibodies or in combination with PD-1 blockade was accompanied by an increased frequency of effector CD4$^+$ and CD8$^+$ T cells infiltrating the tumours of antibody-treated animals, without affecting B cell or regulatory T (T_{reg}) cell infiltration (Extended Data Fig. 5m) and with an induction of a larger fraction of granzyme B$^+$CD8$^+$ T cells and TNF$^+$IFNγ$^+$ cells among both the CD4$^+$ and CD8$^+$ T cell compartments (Fig. 3e and Extended Data Fig. 5n). Together, these data show that therapeutic antibody blockade of TIM-1 in vivo results in tumour growth control of both transplanted and spontaneous tumour models and requires TIM-1 expression on B cells, but not on other cell types, which is consistent with the phenotype observed in tumour-bearing mice with genetic deletion of *Havcr1* in B cells.

Loss of TIM-1 in B cells enhances effector T cell responses

To investigate how TIM-1 loss in B cells affects tumour growth, we analysed the composition of CD45$^+$ cells in the TME, dLN and ndLN of control or *Havcr1*^{BKO} mice using flow cytometry at 16 days after receiving subcutaneous B16F10 cells (Fig. 4a,b and Extended Data Fig. 6). There was an increased immune cell infiltration in *Havcr1*^{BKO} tumours versus control tumours (Extended Data Fig. 6b), and a significant increase in

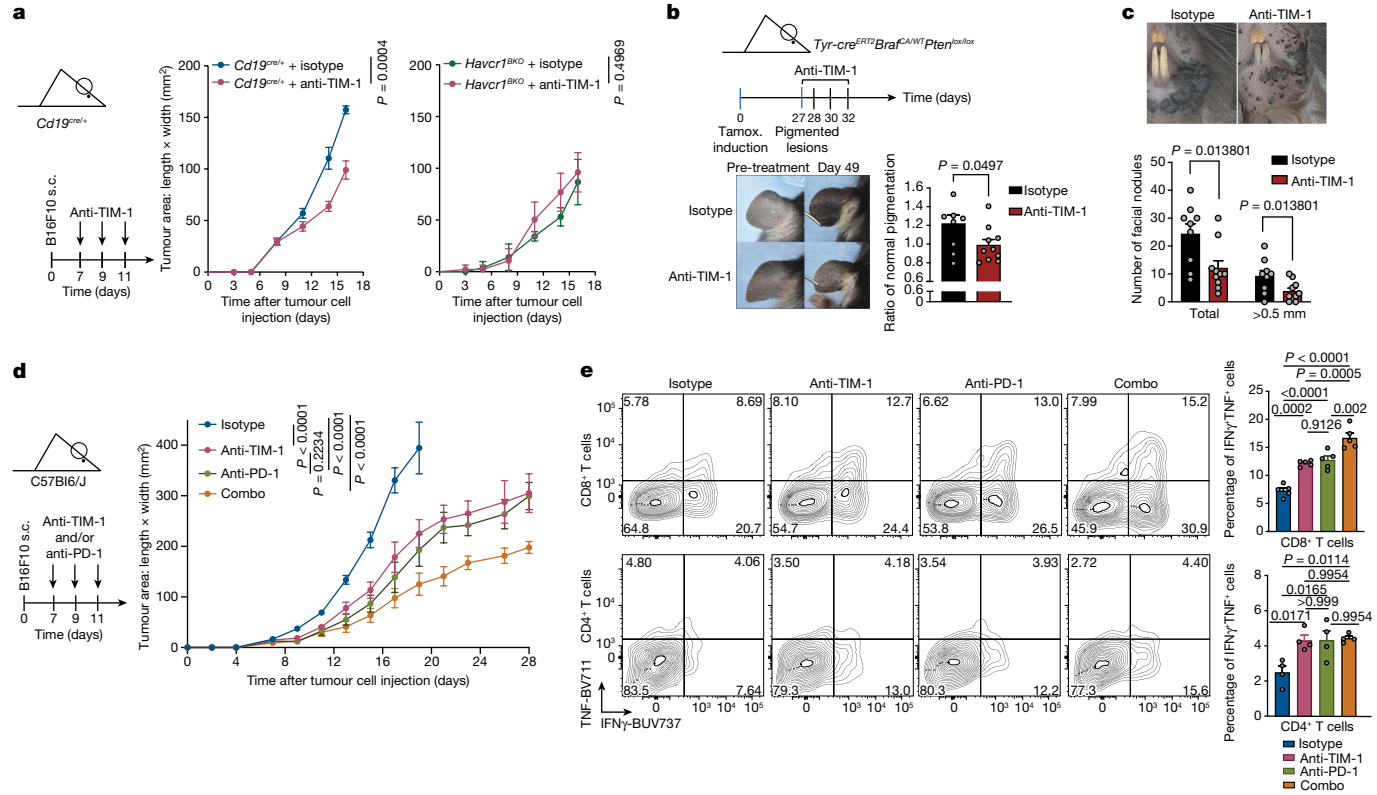

Fig. 3 | Targeting of TIM-1 reduces B16F10 growth, is dependent on TIM-1 expression on B cells and augments PD-1 blockade therapy. a, B16F10 tumour growth in *Cd19*$^{cre/+}$ and *Havcr1*^{BKO} mice ($n = 8$ mice per group) that were treated with anti-TIM-1 or isotype control antibodies. **b**,**c**, *Braf-Pten* mice were painted with 4-hydroxytamoxifen (tamox.) on one ear and treated with anti-TIM-1 antibodies beginning 27 days later when visible lesions were apparent. Representative photographs, and measurements of pigmentation (**b**) and the number of facial nodules (**c**) are shown for isotype-treated ($n = 9$ mice) or anti-TIM-1-treated ($n = 10$ mice) ears at treatment and 3 weeks after treatment initiation/7 weeks after tumour induction. Data are mean ± s.e.m. pooled from two to three independent experiments. **d**,**e**, Tumour growth (**d**) and flow cytometry immunophenotyping of TILs showing the frequencies of IFNγ$^+$TNF$^+$ cells among CD8$^+$ and CD4$^+$ TILs (**e**) of C57Bl/6J mice implanted with B16F10 melanoma and treated with anti-TIM-1, anti-PD-1, anti-TIM-1 + anti-PD-1 (combo) or isotype controls. $n = 8$ mice per group for tumour growth analysis and $n = 5$ mice per group for flow cytometry analysis. Statistical analysis was performed using repeated-measures two-way ANOVA (**a** and **d**) and one-way ANOVA with Tukey's multiple-comparison test (**e**).

the frequency of CD8$^+$ T cells, and decreased frequency of FOXP3$^+$CD25$^+$ cells (T_{reg} cells) among CD4$^+$ T cells, resulting in an approximately four-fold increase in the ratio of CD8$^+$ T cells to T_{reg} cells (Extended Data Fig. 6c–e). Moreover, there was a decreased proportion of T_{reg} cells within the dLN of *Havcr1*^{BKO} mice (Extended Data Fig. 6k). Myeloid cell subsets and B cells were unchanged in either the tumour or the LNs (Extended Data Fig. 6f). Moreover, among TILs from *Havcr1*^{BKO} mice, a larger fraction of CD8$^+$ and CD4$^+$ T cells secreted both TNF and IFNγ in tumours compared with the control mice, and CD8$^+$ T cells displayed a stronger cytotoxic profile, with elevated expression of CD107a and an increased frequency of CD8$^+$ T cells co-expressing granzyme B and perforin or the transcription factors EOMES and TBET that regulate IFNγ production (Fig. 4a,b and Extended Data Fig. 6f,g). However, IL-2 production was not changed in CD4$^+$ or CD8$^+$ cells (Fig. 4a), and there were no alterations in TCF1 expression levels or in the co-expression of the checkpoint molecules PD-1 and TIM-3 (Extended Data Fig. 6h,i). Similar results were obtained in mice that received MC38 colon adenocarcinoma (Extended Data Fig. 6l).

To further characterize these changes in the tumours of *Havcr1*^{BKO} mice, we profiled 11,884 CD45$^+$ cells infiltrating the tumours, dLN and ndLN from these mice by combined single-cell RNA- and TCR-seq (scRNA/TCR-seq; Fig. 4c,d and Extended Data Fig. 7a,b). scRNA-seq confirmed an increase in cytotoxic CD8$^+$ T cell infiltration in *Havcr1*^{BKO} tumours versus the controls and showed a higher frequency of clonally expanded CD8$^+$ T cells in *Havcr1*^{BKO} tumours on the basis of TCR analysis (30.3% versus 11.7% of clones with more than 2 cells) (Fig. 4e, Methods and Extended Data Fig. 7c). Notably, clonally expanded CD8$^+$ T cells from *Havcr1*^{BKO} tumours displayed a higher expression of genes associated with an effector/cytotoxic phenotype (that is, *Gzmb*, *Gzma*, *Gzmc*, *Prf1*, *Ifng* and *Ccl4*) (Fig. 4f,g and Extended Data Fig. 7d). Consistently, TILs from B16-OVA-bearing mice showed an increased frequency of proliferating OVA-specific CD8$^+$ T cells in *Havcr1*^{BKO} tumours versus the control as determined by H-2K^b-OVA$_{257–264}$ dextramer staining and Ki-67 expression (Fig. 4h). Taken together, these data indicate that the deletion of *Havcr1* in B cells resulted in decreased T_{reg} infiltration and increased clonally expanded antigen-specific CD8$^+$ TILs.

TIM-1 restrains B cell antigen presentation

To determine the mechanism by which *Havcr1* deletion in B cells influenced T-cell-mediated anti-tumour responses, we analysed the B-cell-intrinsic effects of the genetic loss of *Havcr1*. Although there were no differences in the total frequency of B cells in *Havcr1*^{BKO} tumours, dLNs and ndLNs relative to their respective controls (Extended Data Fig. 8a), scRNA-seq profiles of *Havcr1*^{BKO} B cells from dLNs and tumours (but not ndLNs) had a higher expression of signatures of the response to type I and type II interferons (Fig. 5a–c and Extended Data Figs. 9a and 10a; for example, *Ifnar2*, *Irf1*, *Irf9*, *Stat1* and *Stat2*). Type I interferons are critical regulators of B cell homeostasis and responses[32,33] and potentiate BCR-driven activation, co-stimulation and antigen presentation pathways in B cells[32,34]. Consistently, we found significant enrichment for BCR signalling (not shown), B cell activation (*Lyn*, *Tnfrsf13c*, *Btla*,

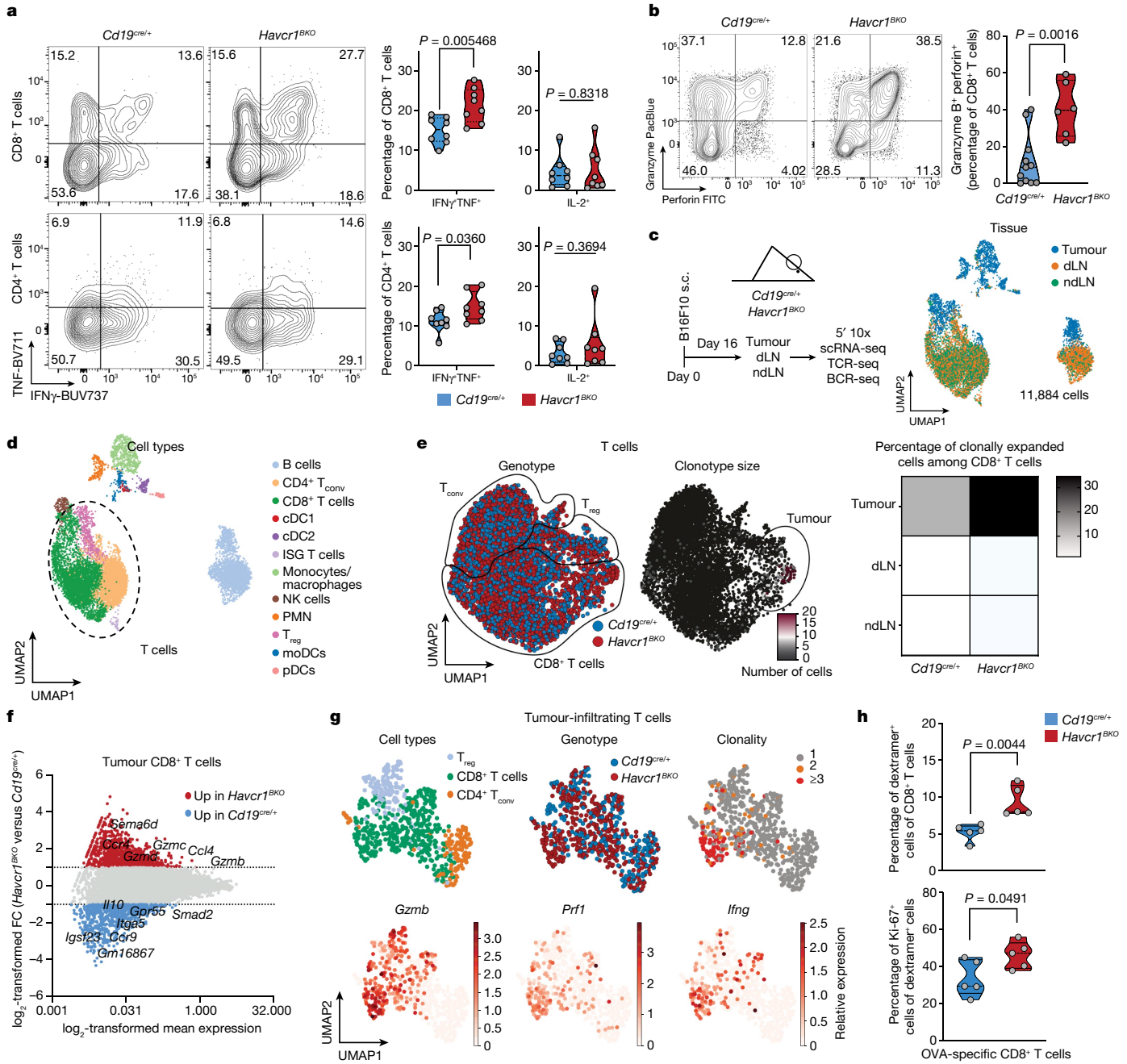

Fig. 4 | *Havcr1* deletion in B cells enhances anti-tumour T cell immunity. **a**,**b**, Flow cytometry analysis of TILs derived from *Cd19*$^{cre/+}$ and *Havcr1*^{BKO} mice implanted s.c. with B16F10. **a**, Representative FACS plot and the percentage of IFNγ and TNF double-positive cells and IL-2 within tumour-infiltrating CD8$^+$ (top) and CD4$^+$ (bottom) T cells. $n = 8$ mice per group. **b**, Representative FACS plot and the percentage of granzyme B and perforin double-expressing CD8$^+$ T cells. $n = 11$ control and $n = 6$ *Havcr1*^{BKO} mice. **c**–**g**, scRNA/BCR-seq and TCR-seq analysis of the TME, dLNs and ndLNs from *Cd19*$^{cre/+}$ and *Havcr1*^{BKO} mice bearing B16F10 melanoma. **c**,**d**, Schematic of the experimental design and UMAP analysis of 11,884 CD45$^+$ cells coloured by their tissue of origin (**c**) and immune cell types (**d**). ISG, IFN-stimulated gene; moDCs, monocyte-derived dendritic cells; PMN, polymorphonuclear leukocytes. **e**, UMAP projection of *Cd19*$^{cre/+}$ (blue) and *Havcr1*^{BKO} (red) T cells delineated between CD4$^+$ conventional T cells, T_{reg} cells and CD8$^+$ T cells (left) and clonally expanded T cells (middle). Right, the frequencies of clonally expanded CD8$^+$ T cells in different compartments. **f**, *MA* plot of gene expression comparing *Cd19*$^{cre/+}$ versus *Havcr1*^{BKO} CD8$^+$ TILs. Positive $\log_2$-transformed fold change corresponds to upregulation within *Havcr1*^{BKO} CD8$^+$ TILs and vice versa. **g**, UMAP analysis of TILs coloured by cell types (top left), genotypes (top middle) and clonal expansion (top right). Bottom, expression of the indicated markers. **h**, The frequencies of OVA-specific cells among CD8$^+$ TILs (top) and Ki-67-expressing OVA-specific CD8$^+$ TILs (bottom). $n = 5$ mice per group. Data are mean ± s.e.m. pooled from at least two to three independent experiments. Statistical analysis was performed using two-tailed Student's *t*-tests (**a**, **b** and **h**).

Cd81 and *Cd22*) and antigen processing and T cell antigen presentation and co-stimulation (*Icosl*, *Cd40* and *Ciita*) gene signatures (Fig. 5a–c and Extended Data Fig. 9b). Supporting these RNA expression patterns, there was increased surface expression of CD86, MHC II and ICOSL on *Havcr1*^{BKO} B cells infiltrating the tumours (Extended Data Fig. 9c). Although *Havcr1* deletion increases the response to type-1 interferons and B cell activation, humoral immunity was largely unaffected by its deletion in the tumour setting. Flow cytometry analysis showed similar frequencies of plasmablasts (B220$^+$CD138$^+$), plasma cells (B220$^{low/-}$CD138$^+$), germinal centre B cells (CD19$^+$GL-7$^+$FAS$^+$) or

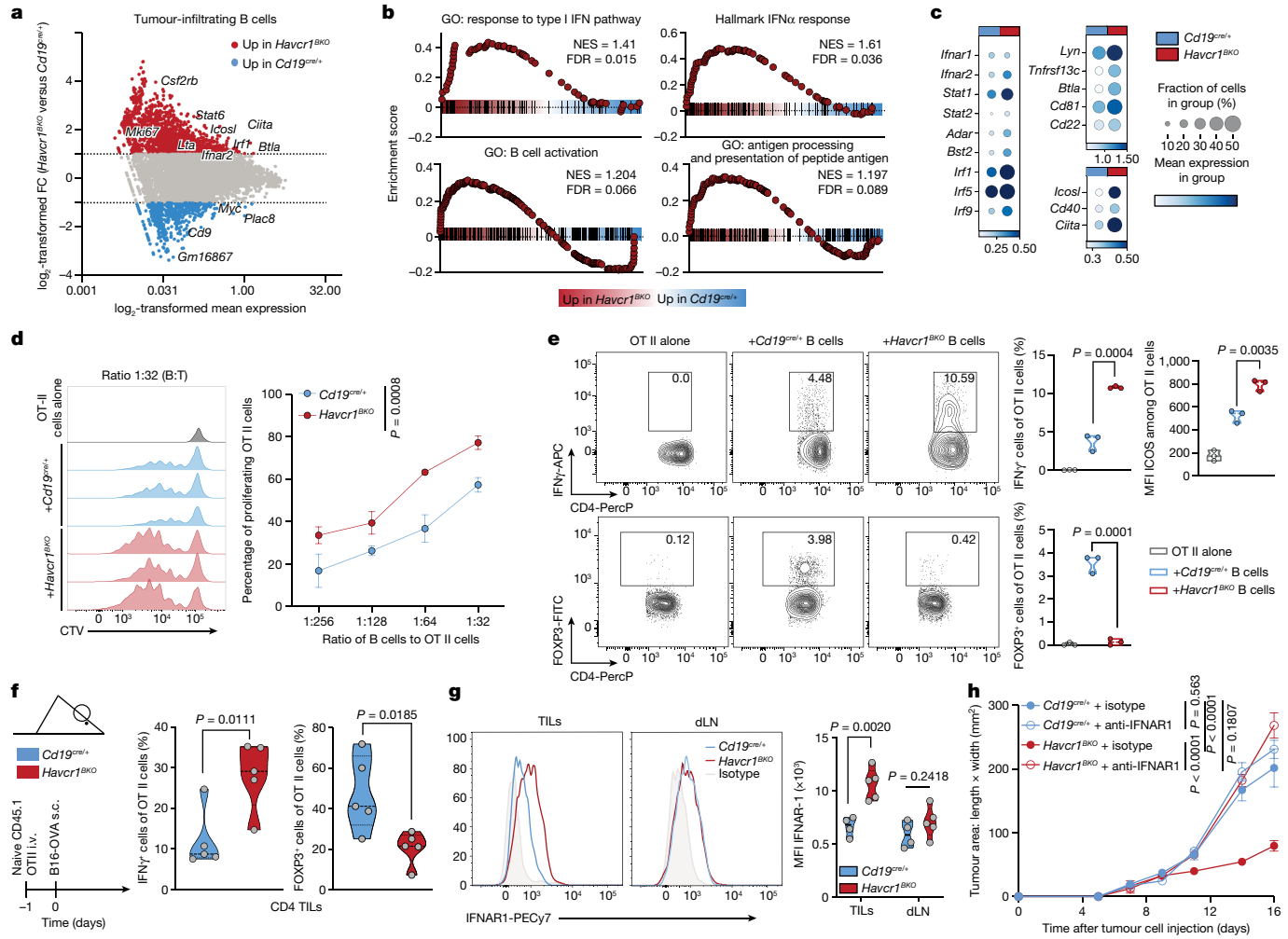

Fig. 5 | TIM-1 deficiency in B cells results in B cell activation, antigen presentation and co-stimulatory function. a–**c**, scRNA-seq analysis of B cells derived from TILs, dLNs and ndLNs of *Cd19*$^{cre/+}$ and *Havcr1*^{BKO} mice bearing B16F10 melanoma. *MA* plot of gene expression comparing tumour-derived *Cd19*$^{cre/+}$ and *Havcr1*^{BKO} B cells (**a**), gene set enrichment analysis (GSEA) analysis (**b**) and dot plots depicting selected genes (**c**) between tumour-infiltrating *Havcr1*^{BKO} and *Cd19*$^{cre/+}$ B cells. Selected genes are annotated. NES, normalized enrichment score. **d**, $OVA_{323–339}$ peptide-pulsed *Havcr1*^{BKO} and *Cd19*$^{cre/+}$ B cells were co-cultured with CellTrace Violet (CTV)-labelled OVA-restricted CD4$^+$ T cells (OT II) at different ratios for 4 days. T cell proliferation was determined by dilution of CTV. Representative histograms and quantitative analysis of the proliferation indices are shown. $n = 3$ mice per group. **e**, T cells were analysed for expression of IFNγ, ICOS and FOXP3. Representative and quantitative data are shown. The circles denote data points from individual mice. $n = 3$. **f**, Naive CD45.1$^+$ OVA-restricted CD4$^+$ T cells were transferred i.v. 1 day before B16-OVA melanoma cell s.c. implantation into CD45.2$^+$ *Cd19*$^{cre/+}$ and *Havcr1*^{BKO} mice. $n = 5$ mice per group. Tumour-infiltrating OT II cells were examined for expression of IFNγ and FOXP3. A schematic of the experimental and quantitative results is shown. **g**, Quantification and representative histogram of IFNAR1 surface expression of B cells derived from TILs and dLNs of *Cd19*$^{cre/+}$ and *Havcr1*^{BKO} mice implanted s.c. with B16F10. $n = 5$ mice per group. **h**, Tumour growth in the indicated mice implanted with B16F10 melanoma and treated with isotype control ($n = 3$ mice per group) or neutralizing anti-IFNAR1 ($n = 4$ mice per group) antibodies. Data are mean ± s.e.m. pooled or representative of at least two to three independent experiments. Statistical analysis was performed using repeated-measures two-way ANOVA (**d** and **h**) and two-tailed Student's *t*-tests (**e**–**g**).

T follicular helper cells within the dLN and spleen from *Havcr1*^{BKO} and control mice (Extended Data Fig. 8b–d,k–m). Furthermore, we did not observe significant differences in circulating immune complexes[35] or in the total amount of IgGs, IgA or IgM in the serum of either naive or B16F10-bearing *Havcr1*^{BKO} and control mice (Extended Data Fig. 8e–h). Importantly, the levels of B16F10-reactive IgGs and IgM were also unaltered in *Havcr1*^{BKO} sera (Extended Data Fig. 8i). Finally, we did not detect a significant increase in class-switched or clonally expanded B cells across the compartments, and there was no difference in major B cell subsets in *Havcr1*^{BKO} mice or mice treated with anti-TIM-1 monoclonal antibodies (Extended Data Fig. 8j–m). Thus, *Havcr1* deletion had little to no effect on humoral immunity in tumours and lymphoid organs.

On the other hand, *Havcr1* deletion enhanced B cell antigen presentation to CD4$^+$ T cells, expanded CD4$^+$ helper T cells and reduced FOXP3$^+$ T_{reg} cell expansion. Indeed, in vitro, *Havcr1*^{BKO} B cells induced greater T cell proliferation in a manner dependent on MHC II presentation (Fig. 5d and Extended Data Fig. 9d,e). Moreover, in vivo MHC II blockade abolished the enhanced anticancer efficacy in *Havcr1*^{BKO} mice, suggesting a critical role for antigen presentation through MHC II in mediating tumour control in mice lacking TIM-1 in B cells (Extended Data Fig. 9f). Notably, *Havcr1*^{BKO} B cells also influenced CD4$^+$ T cell expansion and function as *Havcr1*^{BKO} B cells induced a greater fraction of IFNγ$^+$ cells, including a substantial increase of ICOS expression, while inhibiting FOXP3 expression in CD4$^+$ T cells (Fig. 5e). This effect on T cell polarization was recapitulated in vivo by adoptively transferring naive CD4$^+$ T cells from CD45.1 OT-II donors into congenic CD45.2 *Havcr1*^{BKO} or control mice (Fig. 5f and Extended Data Fig. 9g). Tumour-derived CD45.1$^+$CD4$^+$ T cells in *Havcr1*^{BKO} hosts exhibited increased expression

of IFNγ and reduced FOXP3 expression (Fig. 5f). Moreover, whereas FOXP3$^-$ OT II cells exhibited similar proliferative ability in *Havcr1*^{BKO} or control tumours, FOXP3$^+$ OT II cell proliferation was reduced in *Havcr1*^{BKO} tumours (Extended Data Fig. 9g), indicating that T_{reg} cell proliferation is impaired in the TME of *Havcr1*^{BKO} tumours. Moreover, *Havcr1*^{BKO} B cells expressed higher levels of the costimulatory ligand ICOSL both in vitro and ex vivo (Extended Data Fig. 9c,d), a recently described marker of anti-tumour B cells, potentiating T-cell-mediated anticancer immunity[36].

Enhanced IFN type I and II sensing in TIM-1-deficient B cells

During B cell activation, antigen presentation and expression of co-stimulatory molecules such as ICOSL are tightly regulated by the type I and type II IFN signalling cascade, influencing B cell–T cell cooperation and effector T cell responses. In tumours, *Havcr1*^{BKO} B cells exhibit a marked enrichment for a type I IFN gene signature, enhanced IFN-β responsiveness and substantially increased expression of IFNα/β receptor (IFNAR), comprising the IFNAR1 and IFNAR2 chains, ex vivo (Fig. 5c,g). We hypothesized that TIM-1 expression on B cells during activation suppresses the type I interferon response and, as a result, limits B cell activation and antigen presentation ability. Indeed, activation of wild-type B cells (*Cd19*$^{cre/+}$) with anti-IgM and anti-CD40 increases the expression of TIM-1 on B cells (Extended Data Fig. 9h), but IFNβ limits TIM-1 upregulation with a significantly increased surface expression of CD86 and MHC II in *Havcr1*^{BKO} B cells after anti-IgM and anti-CD40 stimulation (Extended Data Fig. 9h). These data suggest an interplay between the TIM-1 and type I interferon pathways in that increased TIM-1 expression limits the response to type 1 interferons and, conversely, type 1 interferons limit TIM-1 expression on B cells and increase B cell activation, supporting antagonism between the two pathways.

We postulated that enhanced IFNAR signalling could regulate the anti-tumour immune response of *Havcr1*^{BKO} B cells, and treated B16F10-tumour-engrafted control and *Havcr1*^{BKO} mice with either anti-IFNAR1 or isotype control antibodies. IFNAR1 blockade completely abrogated tumour growth control observed in *Havcr1*^{BKO} mice (Fig. 5h), and inhibited the increased CD8$^+$ T cell abundance normally observed in the TILs of *Havcr1*^{BKO} mice, but did not affect T_{reg} or IFNγ$^+$CD4$^+$ T cell proportions in *Havcr1*^{BKO} mice (Extended Data Fig. 9i). Furthermore, tumour-derived leukocytes from anti-IFNAR1-treated *Havcr1*^{BKO} mice displayed decreased B cell infiltration and lower expression of MHC I, MHC II and CD86 on the B cell surface (Extended Data Fig. 9j). Finally, projection of the intratumoural *Havcr1*^{BKO} B cell signature onto the single-cell profiles of human melanoma-infiltrating B cells obtained from ICB responder versus non-responder samples[20] marked a distinct cluster of *Havcr1*^{BKO} B cells overlapping with B cells derived from the patients who responded but not in the B cells from patients who did not respond to anti-PD-1 therapy (Extended Data Fig. 9k). Furthermore, the type I interferon response or antigen processing and presentation signatures were increased in B cell clusters (particularly cluster 4) from responders of ICB therapy and particularly the ones enriched for the *Havcr1*^{BKO} B cell signature, supporting a potential role of these pathways in promoting anti-tumour immunity in humans (Extended Data Fig. 9l–n). As downstream signalling from interferons converges onto similar pathways, and *Havcr1*^{BKO} B cells from tumours present a high signature score for the response to IFNγ (Extended Data Fig. 10a), we tested whether other interferons could inhibit TIM-1 induction in B cells in vitro. Notably, although IFNλ had no effect on TIM-1 expression, both IFNβ and IFNγ significantly inhibited TIM-1 induction, with a more potent role for IFNβ in both mouse and human B cells (Extended Data Fig. 10b). Moreover, blockade of the IFNγ pathway using anti-IFNGR monoclonal antibodies partially abrogated the protective effects and restored the B16F10 growth in *Havcr1*^{BKO} mice (Extended Data Fig. 10d). Finally, we examined the cellular source of IFNβ in the TME that acts on *Havcr1*^{BKO} B cells and leads to tumour control. IFNβ was found at a high abundance in the TME, consistent with previous reports[37], but was not changed in *Havcr1*^{BKO} mice, and plasmacytoid dendritic cells (pDCs) were the highest IFNβ-expressing cell type in the TME (Extended Data Fig. 10e,f). Moreover, pDC depletion using anti-PDCA1 antibodies abrogated the tumour control observed in *Havcr1*^{BKO} mice, consistent with the anti-IFNAR1 blockade and highlighting the contribution of pDCs as the major source of IFNβ within the TME (Extended Data Fig. 10g–i). Overall, these results suggest that TIM-1 surface expression is regulated by type I and type II interferons. Moreover, TIM-1 expression limited B cell responses in the TME by regulating type I interferon receptor expression/signalling, consequently dampening their ability to present antigen and co-stimulate anti-tumour effector T cells.

Discussion

Whereas the role of T cells in anti-tumour immunity has been exhaustively studied, the role of B cells in anti-tumour immunity remains less well understood, hampering efforts to harness the B cell response for cancer immunotherapy. Here we identified a subset of B cells that co-expressed TIM-1 among several other checkpoint molecules, and the proportion increased with tumour progression in the tumour dLN. Although various checkpoint molecules expressed on B cells have an important intrinsic role in B cell homeostasis and responses[26–29], only the selective deletion of *Havcr1* in B cells profoundly limited tumour growth. In patients with cancer, TIM-1$^+$ B cells also co-expressed multiple checkpoint molecules, suggesting that this co-expression cluster identifies a B cell programme or activation state that is conserved between mice and humans. Importantly, this subset was strongly decreased in the patients with cancer who had received checkpoint blockade therapy. However, our observed association of high TIM-1 expression or immune checkpoint expressing B cells with poor clinical outcome in human cancers requires further study owing to the lack of sufficient B cells captured in human tumour single-cell atlases. Our data also suggest that B cells may have an important role during B and T cell priming within the dLN, before acting locally within the tumour. Analysis of TIM-1$^+$ B cells co-expressing checkpoint molecules within the sentinel LNs of patients with cancer would provide additional insights into the emergence of this B cell subset in human tumours.

Our analysis reveals a critical role for TIM-1 expression by B cells in promoting tumour growth, strengthening our initial findings[38]. The induction of TIM-1 after BCR-driven activation suggests that TIM-1 does not define a separate B cell lineage (Extended Data Fig. 3h). While TIM-1 marks B cells that express IL-10, a key mediator of B cell regulatory function[25,39], loss of IL-10 from B cells had no effect on tumour growth control. Although TIM-1 is also expressed on other cell types[40,41], including T cells as we previously described[42–44], we did not observe changes in tumour burden in mice with conditional deletion of *Havcr1* in T cells, suggesting a B-cell-specific role for TIM-1 in anti-tumour immunity.

Our comprehensive scRNA-seq profiling and functional analysis of the TME reveals two interconnected roles of TIM-1$^+$ B cells: (1) inhibition of anti-tumour CD8$^+$ and CD4$^+$ T cells, limiting the expansion of tumour-specific effector CD8$^+$ T cells; and (2) promotion of regulatory FOXP3$^+$ T cell induction. Notably, the enhanced effector and cytotoxic profiles of T cells from *Havcr1*^{BKO} tumour-bearing mice were not accompanied by an increase in the fraction of stem-like TCF1$^+$ progenitors or a reduction in checkpoint receptor expression on T cells, suggesting a selective promotion of T cell effector function by TIM-1-deficient B cells. TIM-1 expressed on B cells may curtail multiple B cell functions, including antigen presentation, expression of co-stimulatory ligands, inflammatory cytokine production and cytokine responsiveness, which all coordinately promote effector anti-tumour T cell responses.

Our results highlighted a role for TIM-1 in regulating intrinsic B cell activation and function. The humoral response to B16F10 melanoma, which has been shown to either promote tumour growth or clearance

of tumour cells[45], was unaffected by *Havcr1* deletion. However, B cells lacking TIM-1 exhibit an enhanced type I interferon response gene signature that has been described to lower the BCR activation threshold, and to promote B cell antigen presentation and costimulatory functions[32,33,46]. Our data suggest that TIM-1 limits excessive B cell activation, antigen presentation and T cell activation—B cell responses that are associated with a positive outcome in multiple cancers—by fostering intratumoural B cell–T cell cooperation[47–49]. Gene expression of lymphotoxin β (*Ltb*) and *Icosl*, associated with formation of tertiary lymphoid structures, was increased in B cells derived from *Havcr1*^{BKO} tumours (data not shown), suggesting that the enhanced interferon response may promote the development of ectopic lymphoid follicles (tertiary lymphoid structures). This suggests a mechanism whereby the loss of TIM-1 on B cells affects T cell activation and expansion and is reminiscent of recent studies highlighting the cooperation of CD4$^+$ and CD8$^+$ T cells in anticancer immunity, and the formation of tertiary lymphoid structures in effective checkpoint blockade immunotherapy in tumours[50–52]. Particularly, our results set the stage for future investigations regarding the spatial organization of TIM-1$^+$ B cells in tissues and evaluating how this affects tumour growth or the response to ICB in human tumour samples.

In summary, our study identifies TIM-1 as a critical checkpoint of B cell activation. TIM-1 impacts type 1 interferon responsiveness in B cells, limiting B cell activation, antigen-presentation and co-stimulation, thereby highlighting TIM-1 as a potential target by which B cell responses can be unleashed in promoting anti-tumour immunity. Identifying specific checkpoint molecules on B cells, such as TIM-1, may enable the harnessing of this second arm of the adaptive immune system, thereby improving therapeutic efficacy and broadening the application of immune checkpoint blockade in cancer immunotherapy.

Online content

Any methods, additional references, Nature Portfolio reporting summaries, source data, extended data, supplementary information, acknowledgements, peer review information; details of author contributions and competing interests; and statements of data and code availability are available at https://doi.org/10.1038/s41586-023-06231-0.

1. Topalian, S. L. et al. Safety, activity, and immune correlates of anti-PD-1 antibody in cancer. *N. Engl. J. Med.* **366**, 2443–2454 (2012).
2. Wolchok, J. D. et al. Nivolumab plus ipilimumab in advanced melanoma. *N. Engl. J. Med.* **369**, 122–133 (2013).
3. Thorsson, V. et al. The immune landscape of cancer. *Immunity* **48**, 812–830 (2018).
4. Griss, J. et al. B cells sustain inflammation and predict response to immune checkpoint blockade in human melanoma. *Nat. Commun.* **10**, 4186 (2019).
5. Ladanyi, A. et al. Prognostic impact of B-cell density in cutaneous melanoma. *Cancer Immunol. Immunother.* **60**, 1729–1738 (2011).
6. Gupta, N. T. et al. Change-O: a toolkit for analyzing large-scale B cell immunoglobulin repertoire sequencing data. *Bioinformatics* **31**, 3356–3358 (2015).
7. Delaney, C. et al. Combinatorial prediction of marker panels from single-cell transcriptomic data. *Mol. Syst. Biol.* **15**, e9005 (2019).
8. Wolf, Y., Anderson, A. C. & Kuchroo, V. K. TIM3 comes of age as an inhibitory receptor. *Nat. Rev. Immunol.* **20**, 173–185 (2020).
9. Mohib, K., Rothstein, D. M. & Ding, Q. Characterization and activity of TIM-1 and IL-10-reporter expressing regulatory B cells. *Methods Mol. Biol.* **2270**, 179–202 (2021).
10. Xiao, S., Brooks, C. R., Sobel, R. A. & Kuchroo, V. K. Tim-1 is essential for induction and maintenance of IL-10 in regulatory B cells and their regulation of tissue inflammation. *J. Immunol.* **194**, 1602–1608 (2015).
11. Xiao, S. et al. Defect in regulatory B-cell function and development of systemic autoimmunity in T-cell Ig mucin 1 (Tim-1) mucin domain-mutant mice. *Proc. Natl Acad. Sci. USA* **109**, 12105–12110 (2012).
12. Ding, Q. et al. Regulatory B cells are identified by expression of TIM-1 and can be induced through TIM-1 ligation to promote tolerance in mice. *J. Clin. Invest.* **121**, 3645–3656 (2011).
13. Yeung, M. Y. et al. TIM-1 signaling is required for maintenance and induction of regulatory B cells. *Am. J. Transplant.* **15**, 942–953 (2015).
14. Tirosh, I. et al. Dissecting the multicellular ecosystem of metastatic melanoma by single-cell RNA-seq. *Science* **352**, 189–196 (2016).
15. Liu, Y. et al. Immune phenotypic linkage between colorectal cancer and liver metastasis. *Cancer Cell* **40**, 424–437 (2022).
16. Wu, S. Z. et al. A single-cell and spatially resolved atlas of human breast cancers. *Nat. Genet.* **53**, 1334–1347 (2021).
17. Bi, K. et al. Tumor and immune reprogramming during immunotherapy in advanced renal cell carcinoma. *Cancer Cell* **39**, 649–661 (2021).
18. Qian, J. et al. A pan-cancer blueprint of the heterogeneous tumor microenvironment revealed by single-cell profiling. *Cell Res.* **30**, 745–762 (2020).
19. Pelka, K. et al. Spatially organized multicellular immune hubs in human colorectal cancer. *Cell* **184**, 4734–4752 (2021).
20. Sade-Feldman, M. et al. Defining T cell states associated with response to checkpoint immunotherapy in melanoma. *Cell* **175**, 998–1013 (2018).
21. Zhang, L. et al. Single-cell analyses inform mechanisms of myeloid-targeted therapies in colon cancer. *Cell* **181**, 442–459 (2020).
22. Yost, K. E. et al. Clonal replacement of tumor-specific T cells following PD-1 blockade. *Nat. Med.* **25**, 1251–1259 (2019).
23. Bassez, A. et al. A single-cell map of intratumoral changes during anti-PD1 treatment of patients with breast cancer. *Nat. Med.* **27**, 820–832 (2021).
24. Jerby-Arnon, L. et al. A cancer cell program promotes T cell exclusion and resistance to checkpoint blockade. *Cell* **175**, 984–997 e924 (2018).
25. Cerqueira, C., Manfroi, B. & Fillatreau, S. IL-10-producing regulatory B cells and plasmocytes: molecular mechanisms and disease relevance. *Semin. Immunol.* **44**, 101323 (2019).
26. Floudas, A. et al. Pathogenic, glycolytic PD-1$^+$ B cells accumulate in the hypoxic RA joint. *JCI Insight* https://doi.org/10.1172/jci.insight.139032 (2020).
27. Hasan, M. M. et al. Implication of TIGIT$^+$ human memory B cells in immune regulation. *Nat. Commun.* **12**, 1534 (2021).
28. Lino, A. C. et al. LAG-3 inhibitory receptor expression identifies immunosuppressive natural regulatory plasma cells. *Immunity* **49**, 120–133 (2018).
29. Xiao, S. et al. Checkpoint receptor TIGIT expressed on Tim-1$^+$ B cells regulates tissue inflammation. *Cell Rep.* **32**, 107892 (2020).
30. Horikawa, M., Minard-Colin, V., Matsushita, T. & Tedder, T. F. Regulatory B cell production of IL-10 inhibits lymphoma depletion during CD20 immunotherapy in mice. *J. Clin. Invest.* **121**, 4268–4280 (2011).
31. Hilgenberg, E. et al. Interleukin-10-producing B cells and the regulation of immunity. *Curr. Top. Microbiol. Immunol.* **380**, 69–92 (2014).
32. Domeier, P. P. et al. B-cell-intrinsic type 1 interferon signaling is crucial for loss of tolerance and the development of autoreactive B cells. *Cell Rep.* **24**, 406–418 (2018).
33. Le Bon, A. et al. Type I interferons potently enhance humoral immunity and can promote isotype switching by stimulating dendritic cells in vivo. *Immunity* **14**, 461–470 (2001).
34. Hervas-Stubbs, S. et al. Direct effects of type I interferons on cells of the immune system. *Clin. Cancer Res.* **17**, 2619–2627 (2011).
35. Andreu, P. et al. FcRγ activation regulates inflammation-associated squamous carcinogenesis. *Cancer Cell* **17**, 121–134 (2010).
36. Lu, Y. et al. Complement signals determine opposite effects of B cells in chemotherapy-induced immunity. *Cell* **180**, 1081–1097 (2020).
37. Zhou, B., Lawrence, T. & Liang, Y. The role of plasmacytoid dendritic cells in cancers. *Front. Immunol.* **12**, 749190 (2021).
38. Ding, Q., Mohib, K., Kuchroo, V. K. & Rothstein, D. M. TIM-4 identifies IFN-γ-expressing proinflammatory B effector 1 cells that promote tumor and allograft rejection. *J. Immunol.* **199**, 2585–2595 (2017).
39. Zhou, X. CD19$^+$IL-10$^+$ regulatory B cells affect survival of tongue squamous cell carcinoma patients and induce resting CD4$^+$ T cells to CD4$^+$Foxp3$^+$ regulatory T cells. *Oral Oncol.* https://doi.org/10.1016/j.oraloncology.2015.11.003 (2016).
40. de Souza, A. J., Oriss, T. B., O'Malley K, J., Ray, A. & Kane, L. P. T cell Ig and mucin 1 (TIM-1) is expressed on in vivo-activated T cells and provides a costimulatory signal for T cell activation. *Proc. Natl Acad. Sci. USA* **102**, 17113–17118 (2005).
41. Xiao, S. et al. Tim-1 stimulation of dendritic cells regulates the balance between effector and regulatory T cells. *Eur. J. Immunol.* **41**, 1539–1549 (2011).
42. Mariat, C. et al. Tim-1 signaling substitutes for conventional signal 1 and requires costimulation to induce T cell proliferation. *J. Immunol.* **182**, 1379–1385 (2009).
43. Xiao, S. et al. Differential engagement of Tim-1 during activation can positively or negatively costimulate T cell expansion and effector function. *J. Exp. Med.* **204**, 1691–1702 (2007).
44. Meyers, J. H. et al. TIM-4 is the ligand for TIM-1, and the TIM-1-TIM-4 interaction regulates T cell proliferation. *Nat. Immunol.* **6**, 455–464 (2005).
45. Sharonov, G. V., Serebrovskaya, E. O., Yuzhakova, D. V., Britanova, O. V. & Chudakov, D. M. B cells, plasma cells and antibody repertoires in the tumour microenvironment. *Nat. Rev. Immunol.* **20**, 294–307 (2020).
46. Braun, D., Caramalho, I. & Demengeot, J. IFN-α/β enhances BCR-dependent B cell responses. *Int. Immunol.* **14**, 411–419 (2002).
47. Bruno, T. C. et al. Antigen-presenting intratumoral B cells affect CD4$^+$ TIL phenotypes in non-small cell lung cancer patients. *Cancer Immunol. Res.* **5**, 898–907 (2017).
48. Rivera, A., Chen, C. C., Ron, N., Dougherty, J. P. & Ron, Y. Role of B cells as antigen-presenting cells in vivo revisited: antigen-specific B cells are essential for T cell expansion in lymph nodes and for systemic T cell responses to low antigen concentrations. *Int. Immunol.* **13**, 1583–1593 (2001).
49. Rossetti, R. A. M. et al. B lymphocytes can be activated to act as antigen presenting cells to promote anti-tumor responses. *PLoS ONE* **13**, e0199034 (2018).
50. Germain, C., Gnjatic, S. & Dieu-Nosjean, M. C. Tertiary lymphoid structure-associated B cells are key players in anti-tumor immunity. *Front. Immunol.* **6**, 67 (2015).
51. Cabrita, R. et al. Tertiary lymphoid structures improve immunotherapy and survival in melanoma. *Nature* **577**, 561–565 (2020).
52. Helmink, B. A. et al. B cells and tertiary lymphoid structures promote immunotherapy response. *Nature* **577**, 549–555 (2020).

Methods

Mice

C57BL/6J, B6.129S2-Ighmtm1Cgn/J (μMT), B6.129-*Prdm1*^{tm1Clme}/J (*Prdm1*$^{fl/fl}$), Tg(*Cd4-cre*)1Cwi (*Cd4*^{cre}) and B6.129P2(C)-*Cd19*tm1(cre)Cgn/J (*Cd19*^{cre}), B6.Cg-Tg(TcraTcrb)425Cbn/J (OT II), B6.SJL-Ptprca Pepcb/BoyJ (CD45.1) and B6.129S2-*H2*$^{dlAb1\text{-}Ea}$/J (MHC II KO) mice were purchased from Jackson Laboratory and bred in our facility or used for experiments after at least 1 week of housing in our facility. CD45.1 and OT II mice were crossed to generate CD45.1-OT II mice. *Havcr1*$^{fl/fl}$, *Tigit*$^{fl/fl}$, *Havcr2*$^{fl/fl}$, *Pdcd1*$^{fl/fl}$, *Lag3*$^{fl/fl}$ and *Il10*$^{fl/fl}$ mice generated on the C57BL/6 background and described previously[10,29]. *hCD20*^{creERT2} mice[53] were provided by M. Shlomchik. Floxed mice were crossed to *Cd4*^{cre}, *Cd19*^{cre} or *hCD20*^{creERT2} mice in our facility. *Havcr1*$^{+/+}$ or *Havcr1*$^{fl/fl}$ × *hCD20*^{creERT2} (*hCD20*^{TamCre} and TIM-1^{iBKO}) mice were gavaged with 4 mg Tamoxifen in 200 μl corn oil on the days indicated in the figure. While TIM-1$^{fl/fl}$ and *Cd19*$^{cre/+}$ animals had a similar tumour growth profile (not shown), we preferentially used the *Cd19*$^{cre/+}$ mice as controls as this strain has been generated as 'knock-in/knock-out', which partially impairs CD19 expression. *Braf-Pten* mice (B6.Cg-Braf^{tm1Mmcm}Pten^{tm1Hwu}Tg(Tyr-cre/ERT2)13Bos/BosJ) and ZsG mice (B6.Cg-Gt(ROSA)26Sortm6(CAG-ZsGreen1)Hze/J) were purchased from The Jackson Laboratory. Mice used in the inducible cancer model (*Braf-Pten*-ZsG) were crosses of *Braf-Pten* and ZsG bred in-house carrying the following genotype: *Braf*$^{tm1Mmcm+/-}$, *Pten*$^{tm1Hwu+/+}$, Tg(Tyr-cre/ERT2)13Bos^{+} and B6.Cg-Gt(ROSA)26Sortm6(CAG-ZsGreen1)Hze/J$^{+/-}$ or B6.Cg-Gt(ROSA)26Sortm6(CAG-ZsGreen1)Hze/J$^{-/-}$, where the plus (+) indicates presence of the mutant/transgenic allele and a minus (−) indicates allele absence. *ZsG*$^{+/-}$ and *ZsG*$^{-/-}$ mice were included in equal proportions in each treatment group. Mice aged 4–10 weeks were used for experiments. All of the experiments were conducted in accordance with animal protocols approved by the Harvard Medical Area Standing Committee on Animals or BWH and MGH IACUC.

Cell lines

B16F10 mouse melanoma and MC38 mouse colon adenocarcinoma cell lines were obtained from ATCC. B16-OVA cells (B16-F10 cells engineered to express OVA) were provided by K. Wucherpfennig. KP1.9 was derived from lung tumours of C57BL/6 KP mice and was provided by A. Zippelius. All cells were cultured in a humidified, 5% CO_2 incubator at 37 °C, and grown in RPMI or DMEM with 10% fetal bovine serum (FBS) and 100 U ml^{-1} penicillin–streptomycin (Life Technologies). All cell lines were tested and were negative for mycoplasma contamination.

Tumour models

For primary tumour growth experiments, MC38 (1×10^6), B16F10 (2.5×10^5) and B16-OVA (5×10^5) cells were s.c. or intradermally injected into the right flank at a final volume of 100 μl. Tumour growth was measured using digital callipers, and tumour sizes were recorded. For primary tumour cell dissemination experiments, 2×10^5 B16F10 cells were injected i.v. into the tail vein, lungs were collected on day 14 and B16F10 colonies were counted using a dissecting microscope. For lung tumours (KP1.9, containing *Kras* and *Trp53* mutations)[54], 2.5×10^5 cells were injected i.v. in 100 μl PBS to develop orthotopic tumours. Then, 4 weeks after injection, lungs were collected, embedded in paraffin, sectioned (4 μm thickness) and stained with haematoxylin and eosin. Quantification of tumour area was calculated as the percentage of area occupied by the tumour among total lung tissue surface.

Autochthonous mouse melanoma experiments. Tamoxifen induction was initiated when *Braf-Pten* mice were 4 weeks old. To induce tumours, 2 μl of 10 mg ml^{-1} 4-hydroxytamoxifen (Sigma-Aldrich, H6278) dissolved in 100% ethanol was administered to the left ear on three consecutive days. Tumours were allowed to develop for 24–27 days, at which time visible pigmentation was present. The anti-TIM-1 (clone 3B3) treatment schedule is indicated in the figure schematic. Mice were euthanized 3 weeks after initiation of treatment with anti-TIM-1 antibodies. Differences in darkening of the skin were measured by reflective colorimetry (Commission Internationale de l'Eclairage [CIE] L∗ white–black colour axis) using the CR-400 Colorimeter (Minolta) calibrated to a white standard background calibration plate before each set of measurements. Photos were taken using a Nikon D750 DSLR camera with a Nikon Nikkor AF-S Micro 60 mm lens. Photos were taken on manual with settings of shutter speed 1/400 s, aperture f/13, ISO 320. Ott-Lite Model L139AB lamps were used to create uniform lighting for photos. Facial tumour diameters were measured, and the number of tumour nodules was counted manually.

In vivo treatments

In some experiments, mice were treated with 250 μg of anti-TIM-1 (3B3) and/or 200 μg of anti-PD-1 (RMP1-14), anti-MHC II (M5/114), anti-IFNAR1 (MAR1-5A3) or anti-IFNGR (GR-20) antibodies or 250 μg of control immunoglobulin (rat IgG2a) intraperitoneally (i.p.) on days 7, 9 and 11 after tumour implant. For in vivo B cell or pDC depletion, some groups of mice were injected i.v. or i.p. with 250 μg of anti-CD20 (SA271G2) or anti-PDCA1 (927), respectively, or their isotype control (rat IgG2b) with schedules as indicated on the figures or figure legends.

Preparation of cell suspensions

Single-cell suspensions were prepared from mouse LNs, spleens or tumours as previously described[55]. In brief, tumours were dissociated mechanically and digested with 1 mg ml^{-1} collagenase A and 0.1 mg ml^{-1} DNase I for 20 min at 37 °C. LNs and spleens were mechanically dissociated, digested with 0.1 mg ml^{-1} collagenase A and 0.01 mg ml^{-1} DNase I for 20 min at 37 °C, and passed through a 40 μm cell strainer and lysed of red blood cells (using ACK buffer) then washed with cold PBS and centrifuged.

Multiplexing and droplet-based scRNA-seq, scBCR-seq and scTCR-seq

For the B cell atlas analysis or the examination of *Cd19*$^{cre/+}$ and *Havcr1*^{BKO} mice, viable leukocytes were sorted by FACS from tumours (70% CD3e^{+} and CD19^{+} cells, 30% total CD45^{+} cells), dLN and ndLN (100% CD45^{+} cells) at three different timepoints as shown in Extended Date Fig. 2a. For the analysis of TIM-1-expressing B cells, viable B220^{+}CD19^{+}CD138^{+} and B220^{+}CD19^{+}CD138^{-} cells derived from the dLN, ndLN and spleen from C57Bl6/J mice were sorted by FACS. Cells were resuspended in PBS containing 2% FCS and stained with oligo-tagged TotalSeq antibodies (BioLegend) for 30 min on ice. Cells were washed and pooled accordingly, centrifuged at 1,200 rcf for 5 min at 4 °C and resuspended in PBS + 2% FCS. For the B cell temporal profiling, nine samples were combined into each channel of the Chromium system (10x Genomics): tumour, dLN and ndLN from three different timepoints (days 7, 10 and 16) of one replicate. For the examination of *Cd19*$^{cre/+}$ and *Havcr1*^{BKO}, six samples were combined into each channel: tumour, dLN, ndLN derived from one biological replicate of each genotype. For the analysis of TIM-1^{+} cells, cells derived from the LN were loaded in separate channels and the TIM-1^{+} and TIM-1^{-} splenic cells were combined. For samples that did not include scBCR-seq and/or scTCR-seq and 5′ feature barcoding, sorted cells were separated into droplet emulsions using the Chromium Single Cell 3′ Solution (v2) according to manufacturer's instructions (10x Genomics). Samples that included scBCR-seq and/or scTCR-seq and 5′ feature barcoding were separated into droplet emulsions using the Chromium Single Cell 5′ V2 Solution, according to manufacturer's instructions (10x Genomics). scBCR-seq, scTCR-seq and 5′ feature barcoding libraries were prepared according to the manufacturer's instructions (10x Genomics). scRNA-seq libraries (5′ and 3′) and 5′ feature barcoding libraries were sequenced on the Illumina NextSeq 550 using the 75-cycle kit to a depth of 100 million reads per library.

Pre-processing of the droplet-based scRNA-seq data and VDJ-seq time-course dataset

Three sample sets were loaded, each sample set on two separate 10x channels. Sample sets included samples from tumours, dLNs and ndLNs from day 7, day 10 and day 16 after injection. Cells from a separate location and timepoint were hashed separately to be distinguishable in the analysis. Hashed scRNA-seq expression profiles were processed in Terra (https://app.terra.bio/) using the 'demultiplexing' workflow in scCloud/Cumulus (v.0.8.0)[56], a wrapper for cellranger_mkfastq, cellranger_count (v.3.0.2) and cumulus_adt. The profiles were mapped to the prebuilt mouse reference mm10, CellRanger reference v.1.2.0 (Ensembl v84 gene annotation), specifying that the profiles were obtained with the 10x 5′ chemistry. After mapping, cell profiles were processed to remove ambient RNA with CellBender[57] through the Terra workflow 'run_cellbender_remove_background_gpu', with Docker image 'us.gcr.io/broad-dsde-methods/cellbender:latest' (as of 30 January 2020) with epochs = 300, low-count-threshold = Null, expected-cells: 15000 (Timecourse_1, repl1&2), 3000 (Timecourse2_repl1&2) or 7000 (Timecourse3_repl1&2). Next, cell profiles were matched with antibody-derived tag counts to assign their identity, as samples from different timepoints or locations had been associated with unique combinations of two hashing antibodies. Cells with incorrect combinations of hashing antibodies were discarded from the analysis. Separately, reads from the VDJ libraries (BCR and TCR) were processed with Cumulus, using the prebuilt reference GRCm38_vdj_v3.1.0, part of CellRanger reference v.3.1.0, annotation built from Ensembl Mus_musculus.GRCm38.94.gtf. Filtered_contig annotations and filtered_contig.fasta from the two separate channels of each sample set (technical replicates) were merged before further processing.

RNA profiles were then processed with Scanpy (v.1.7.2). Cells were filtered out if their fraction of mitochondrial genes was ≥4.5% or if they had <1,000 counts or <300 or >6,000 genes. Genes detected in ≤1 cell were also filtered out. Each cell transcriptome was scaled to sum to 10,000, and expression values were further normalized with log1p, finally obtaining log[TP10K + 1] values for each gene. Scrublet[58] was run to detect doublets and only cells with a doublet score of <0.5 were retained for the analysis. Highly variable genes were selected using the highly_variable_genes function in scanpy, with min_mean=0.01, max_mean=3, min_disp = 0.25. Normalized values were then scaled to unit variance with a max_value for standard deviation equal to 10. Dimensionality reduction with UMAP, using a *k*-nearest neighbour graph ($k = 15$), was performed after batch correction using Harmony[59] (using the harmony-pytorch wrapper) on biological replicates. Cells from the dLN and ndLN at day 16, in the third biological replicate, clustered separately from cells from the other two biological replicates even after batch correction and displayed higher expression of ribosomal genes and genes associated with oxidative stress. We removed these samples from the analysis. Furthermore, around 300 cells were identified as potential doublets from the expression of markers from different cell types (that is, *Cd19*/*Lyz2*, *Cd19*/*Cd3e* or *Cd4*/*Cd8*) and were excluded from the analysis. Pre-processing described above was repeated after removing these cells from the dataset. Finally, the dataset included 34,071 cells, 17,763 genes with 1,658 genes identified as highly variable genes.

A B-cell-only embedding was obtained repeating the same processing described above starting from only single cells annotated as B cells in the full time-course dataset, with the exception of $n = 5$ in sc.pp. neighbours.

Pre-processing of the droplet-based scRNA-seq data and VDJ-seq *Havcr1*^{BKO} dataset

Hashed transcriptional profiles from three sample sets of *Cd19*$^{cre/+}$ and *Havcr1*^{BKO} samples (each sample set including cells from tumour, dLN and ndLN from a *Cd19*$^{cre/+}$ and *Havcr1*^{BKO} replicate, each loaded onto a single 5′ channel) were processed in Terra with scCloud/Cumulus (v.0.8.0) as described for the time-course dataset above. After mapping, cell profiles were processed to remove ambient RNA with CellBender[57] (latest version as of 30 January 2020) as described above, with expected-cells at 5,000 (replicate 1), 10,000 (replicate 2) and 1,000 (replicate 3). Cells with incorrect combinations of hashing antibodies were discarded from the analysis. Reads from the VDJ libraries (BCR and TCR) were processed using Cumulus, as described for the time-course dataset. RNA profiles were processed using Scanpy (v.1.7.2). Cells were filtered out if their fraction of mitochondrial genes was ≥7.5% or if they had <500 or >5,000 counts, or <300 or >5,000 genes. Genes detected in less than three cells were also filtered out. Each cell profile was scaled to sum to 10,000 and gene expression values were further normalized with log1p, finally obtaining log (TP10K + 1) values for each gene. Scrublet[58] was run to detect doublets and only cells with a doublet score of <0.5 were retained for the analysis. Highly variable genes were selected using the highly_variable_genes function in scanpy, with min_mean = 0.05, max_mean = 3, min_disp = 0.2 run in each individual replicate. Only genes identified as variable in at least two batches were retained. Normalized values were then scaled to unit variance with a max_value for standard deviation equal to 10. Dimensionality reduction with UMAP, using a *k*-nearest neighbours graph ($k = 15$) was performed after batch correction with Harmony[59] (using the harmony-pytorch wrapper) on biological replicates. Finally, the dataset included 11,884 cells, 15,337 genes with 1,668 genes identified as highly variable genes.

A T-cell-only embedding was obtained repeating the same process described above starting only from single-cell profiles annotated as T cells in the full *Cd19*$^{cre/+}$ and *Havcr1*^{BKO} dataset with the exception of the harmonization.

Pre-processing of the droplet-based scRNA-seq TIM1^{+}/TIM1^{-} dataset

scRNA-seq profiles from B cells from dLNs and ndLNs, sorted for TIM-1 surface presence and processed in four separate 10x channels were processed in Terra scCloud/Cumulus (v.0.10.0) as described above, specifying 10x 3′ V2 chemistry. After mapping, cell profiles were processed to remove ambient RNA using CellBender[57] (latest version as of 12 February 2020) as described above, with expected cells at 2,500 (dLN_T1p), 2,500 (nLN_T1n) and 700 (nLN/nLN_T1p).

scRNA-Seq profiles from B cells from the spleens of tumour-bearing mice, sorted for TIM-1 surface presence and hashed together, were also processed in Terra with scCloud/Cumulus (v.0.8.0) as described above, specifying that the profiles were obtained with the 10x 3′ V2 chemistry. After mapping, cell profiles were processed to remove ambient RNA with CellBender[57] (latest version as of 30 Jan 2020) as described above, with expected cells: 12000. scRNA-seq profiles were then processed with Scanpy (v.1.7.2). Cells were filtered out if their fraction of mitochondrial genes was ≥7.5% or if they had <500 or >25,000 counts, or <200 or >5,000 genes. Genes detected in ≤1 cell were also filtered out. Each cell profile was scaled to sum to 10,000 and gene expression values were further normalized with log1p, finally obtaining log (TP10K + 1) values for each gene. Scrublet[58] was run to detect doublets and only cells with a doublet score of <0.5 were retained for the analysis. Highly variable genes were selected using the highly_variable_genes function in Scanpy, with min_mean = 0.0125, max_mean = 3, min_disp = 0.35. Normalized values were then scaled to unit variance with a max_value for a standard deviation equal to 10. Dimensionality reduction with UMAP, using a *k*-nearest neighbours graph ($k = 15$), was performed after regressing out with Harmony[59] (using the harmony-pytorch wrapper), the tissue of origin (dLN, ndLN, spleen) and differences in sample processing (hashed versus non-hashed samples).

A small number (<100) of possible contaminant cells expressing *Lyz2* and *Timd4* were excluded from the analysis, and the dataset was reprocessed as described above.

Finally, the dataset included 13,067 cells, 15,284 genes with 2,215 genes identified as highly variable genes.

Scoring cells using signature gene sets

To calculate a score for a specific set of genes in a given cell, B cell lineage signatures in Supplementary Table 1, signatures obtained from MSigDB[60,61] or other sources as indicated in the figures, we computed scores using scanpy (tl.score_genes). The signature score for each cell was then defined as the average expression of a set of genes subtracted with the average expression of a reference set of genes randomly sampled from the gene pool for each binned expression value.

Differentially expressed genes in scRNA-seq

Differential expression analysis was performed using two-sided *t*-tests or Wilcoxon rank-sum tests as indicated using scanpy's rank_genes_groups function. Subsequently, genes were retained if the fraction of expressing cells within the considered group was ≥0.1, the fraction of expressing cells in the other group was ≤0.95 and the fold change between groups was at least 2 (Extended Data Fig. 3h) or 1 (Figs. 4f and 5a). We considered genes with a Benjamini–Hochberg FDR of <0.05 as significant in Extended Data Fig. 3h. The ranked gene lists for cluster 3 B cells from the time-course dataset and *Havcr1*^{BKO} B cells derived from tumour, dLN and ndLN are shown in Supplementary Tables 2 and 5.

Surface marker prediction using COMET

COMET[7] was applied to predict cell surface markers for clusters of interest. The mouse surfaceome[62] gene list was used, and other parameters were set to default.

Analysis of scTCR-seq data

TCR sequences for each single T cell were assembled using the CellRanger vdj pipeline (v.3.1.0) as described above, leading to the identification of CDR3 sequences and the rearranged TCR gene. TCR repertoire analysis was performed using Scirpy[63] (v.4.2). TCR diversity and TCR clonal size were estimated using scirpy.tl.alpha_diversity and scirpy.pl.clonal_expansion (performing the normalization), respectively. V(D)J gene usage was estimated with scirpy.pl.vdj_usage.

Analysis of scBCR-seq data

BCR sequences for each single B cell were assembled using the CellRanger vdj pipeline (v.3.1.0) as described above. V, D, J chain assignment and clonal group definition was performed using Immcantation[6], run using the provided Docker container image (v.4.1.0), according to the recommendations for 10x datasets from the tutorial, specifying species « mouse » and a conservative distance threshold « 0.1 ».

Analysis of published scRNA-seq studies of human cancer

Processed scRNA-seq data were obtained from previously published, publicly available datasets and are shown in Supplementary Table 4. These datasets included tumour-derived leukocytes isolated before and/or after ICB, from both responding and non-responding patients. We preferentially included count data that had been generated using plate-based platform Smart-seq2, for a higher sequencing depth and better capture of *HAVCR1* transcripts. However, owing to the limited availability of Smart-seq2-generated datasets with a design relevant to the current study, we also selected datasets that had been generated using droplet-based platforms (e.g. 10x Genomics Chromium). For downstream analysis, datasets from these respective protocols were analysed separately. All datasets were used without any change to processing, using the same expression values and cell annotations as originally reported. Moreover, we obtained published and processed scRNA-seq data from ICB responders or non-responders[24] from the Gene Expression Omnibus (GEO: GSE120575). B cells and plasma cells were identified on the basis of the expression of *CD19*, *CD79a*, *CD79b*, *SDC1*, *JCHAIN* and *PRDM1*, then subclustered and processed as described above. For some analysis, the human orthologues of selected genes or *Havcr1*^{BKO} B cell signature gene were determined with the Ensembl project's Biomart database (Ensembl v.101). The signature score was defined as the relative average expression of the orthologue genes of the signature of tumour-infiltrating *Havcr1*^{BKO} B cells, GO response to type I IFN (GO: 0034340) and GO antigen processing and presentation of peptide antigen (GO: 0048002) as computed using scanpy (tl.score_genes). The cell density of the depicted categories was shown by sc.tl.embedding_density (Extended Data Figs. 4j and 9k).

Merging, integrating and clustering of Smart-seq2 datasets

For each Smart-seq2 scRNA-seq dataset, transcripts per million (TPM) count tables and metadata (including quality control metrics, cell type assignment, ICB treatment status) were obtained directly from the original publications or through the Single Cell Portal from the Broad Institute (https://singlecell.broadinstitute.org/single_cell). B cells were selected from each dataset, with selection based on the original annotation as provided by the authors. Although we did not change the pre-processing of the cells, we did remove genes that were expressed in less than two cells to exclude artifacts and redundantly expressed genes. Similarly, mitochondrial and ribosomal protein transcripts marked with the prefix 'MT-' and 'RP-' were discarded.

The individual datasets were merged using 'AnnData.concatenate()' and the normalized counts were subsequently log1p-transformed. Highly variable genes among the concatenated dataset were identified using scanpy's highly_variable_genes() function, with the mean-normalized expression set between 0.5 and 3, and a quantile-normalized variance of >0.5. Normalized values were scaled to unit variance with a maximum standard deviation set to 10. We ran principal component analysis of the highly variable genes and subsequently used harmony_integrate() from Harmony to correct for batch effects between the different datasets. We next computed a *k*-nearest neighbour graph, with the number of neighbours set to 20, followed by dimensionality reduction using UMAP. Cells were clustered using the Leiden algorithm, an improved version of the Louvain algorithm, with a clustering resolution of 1.2. The default values were used for the remaining parameters. The resulting dataset included 2,615 cells, 10,687 genes with 1,618 genes identified as highly variable genes, divided among six clusters.

Merging, integrating and clustering of data from droplet-based platforms (10x Genomics Chromium)

For each 10x scRNA-seq dataset, gene transcript count tables and metadata (including quality control metrics, cell type assignment, ICB treatment status) were obtained directly from the original publications or through the Single Cell Portal from the Broad Institute (https://singlecell.broadinstitute.org/single_cell). B cells were selected from each dataset, with selection based on the original annotation as provided by the authors. Although we did not change the pre-processing of the cells, we did remove genes that were expressed in less than two cells to exclude artifacts and redundantly expressed genes. Similarly, mitochondrial and ribosomal protein transcripts marked with the prefix 'MT-' and 'RP-' were discarded.

The individual datasets were merged using 'AnnData.concatenate()'. Expression values were normalized to sum 10,000 reads per cell and the normalized counts were subsequently log1p-transformed. Highly variable genes among the concatenated dataset were identified using scanpy's highly_variable_genes() function, with the mean-normalized expression set between 0.00125 and 3, and a quantile-normalized variance of >0.5. Normalized values were scaled to unit variance with a maximum standard deviation set to 10. We next ran principal component analysis of the highly variable genes and used harmony_integrate() from Harmony to correct for batch effects between the different datasets. We next computed a *k*-nearest neighbour graph, with the number of neighbours set to 25, followed by dimensionality reduction using UMAP. Cells were clustered

using the Leiden algorithm, an improved version of the Louvain algorithm, with the resolution of clustering of 1.2. The default values were used for the remaining parameters. The resulting dataset included 110,064 cells, 16,313 genes with 2,008 genes identified as highly variable genes.

Differential abundance analysis

To explore the differential abundance of each cluster between the treatment-naive cohort and post-treatment group, the MiloR R package was used. Specifically, we used a predesigned pipeline that allowed interoperability between the R version of Milo with Python-compatible anndata objects according to the following code depicting by the authors of an algorithm available at GitHub (https://github.com/MarioniLab/milo_analysis_2020/blob/main/notebooks/milo_in_python.ipynb). Before running the pipeline, we selected only cells derived from patients with cells from both the before- and after-treatment conditions. One dataset[21] did not contain both timepoints and was excluded from further differential abundance analysis. Likewise, cells of which the timing of acquisition was unclear were discarded. The remaining cells were used to recompute a *k*-nearest neighbour graph, with the number of nearest neighbours set to 10, and the number of reduced dimensions set to 40. Subsequently, cell neighbourhoods were computed using miloR's makeNhoods() function, with 10% of the cells, the value of *k* set to 5 and a number of reduced dimensions of 30. For each neighbourhood, the fraction of cells derived from the pre-treatment and post-treatment was established. We then used 'calcNhoodDistance()' to calculate the distance between neighbourhoods, followed by differential abundance testing within each neighbourhood using the testNhoods() function. Differentially abundant neighbourhoods (classified as having an FDR-corrected *P* value of lower than 0.05) were assigned one of the previously established B cell subtypes when >70% of the cells in the neighbourhood belonged to this specific subset. Neighbourhoods where <70% of the cells belonged to a single B cell subset were annotated as mixed.

Bulk RNA-seq

A total of 1,000 live PAN-B cells ($CD45^+CD3e^-CD138^+$ $CD19^{+/-}$ cells) or TIM-1^+ versus TIM-1^- B cells were double-sorted by FACS and immediately lysed in TCL buffer (QIAGEN) supplemented with 1% β-mercaptoethanol (Sigma-Aldrich). Full-length RNA-seq libraries were prepared according to a modified Smart-seq2 protocol[64] as previously described[65]. cDNA concentration was measured using the Quant-iT PicoGreen dsDNA Assay Kit (Thermo Fisher Scientific) and normalized to 0.25 ng μl^{-1}. cDNA libraries were prepared using the Nextera XT DNA Library Preparation kit (Illumina). The final libraries were confirmed to have a size of 500 bp using a Bioanalyzer (Agilent). Before sequencing, the uniquely barcoded libraries were pooled, normalized to 2 nM and denatured using 0.1 N NaOH. Flow cell cluster amplification and sequencing were performed according to the manufacturer's protocols by the paired-end Illumina sequencing (38 bp × 2) using the 75 cycle NextSeq 500 high output V2 kit (Illumina).

Bulk RNA-seq data analysis

Reads were extracted with Illumina's Bcl2Fastq, run through the KCO (https://usegalaxy.org/) Galaxy server[66]. Reads were mapped and expression of genes was quantified using rsem-1.2.8[67], run from the KCO Galaxy server as above using as annotation 'mm10_ucsc_genomestudio_genes'. Expression was quantified as gene-level TPMs (transcripts per kilobase million). Differential expression analysis and pathway enrichment analysis (Fig. 1l and Extended Data Fig. 1d–g) were performed using iDEP[68] (v.0.92) and DESeq2 (v.1.28.1), respectively. The list of differentially expressed genes between TIM-1^+ and TIM-1^- B cells derived from the dLN is provided in Supplementary Table 3.

GSEA

GSEA[69] was performed for each cell subset based on scores in pre-ranked list mode with 1,000 permutations (nominal *P* value cut-off of <0.05).

Flow cytometry and FACS

Single-cell suspensions were prepared from mouse LNs, spleens or tumours as described above. Live/dead cell discrimination was performed using Live/Dead Fixable viability dye e506 (eBioscience). Surface antibodies used in this study were as follows: CD45 (30-F11), TCRb (H57-597), CD3e (17A2), TCRγδ, CD8a (53-6.7), CD4 (RM4-5), CD19 (6D5), B220, CD138 (281-2), GL-7 (GL-7), FAS (Jo2), IgD (11-26c.2a), IgM (RMM-1), CD21 (CR2/CR1), CD43 (S7), CD93 (AA4.1), CD23 (B3B4), TIM-1 (RMT1-4), Ly6C (HK1.4), Ly6G (1A8), CD11c (N418), CD11b (M1/70), CD64 (X54-5/7.1), CD11c (N418), PD-1 (RMP1-30), TIGIT (1G9), LAG3 (C9B7W), TIM-3 (5D12), CD39 (5F2), CD73 (TY/11.8), CD107a (1D4B), NK1.1 (PK136), MHC I ($H\text{-}2K^b$/$H\text{-}2D^b$, 28-8-6), MHC II (I-A/E, M5/114.15.2), CD80 (16-10A1), CD86 (A17199A), ICOSL (HK5.3), CD40 (3/23), CD25 (3C7), IFNAR1 (MAR1-5A3). The following cell populations were identified on the basis of cell marker expression: $CD4^+$ T cells ($CD45^+TCR\beta^+CD4^+$), $CD8^+$ T cells ($CD45^+TCR\beta^+CD8^+$), B cells ($CD45^+B220^+CD19^+$), natural killer (NK) cells ($CD45^+NK1.1^+$), NKT cells ($CD45^+NK1.1^+TCR\beta^+$), PMN ($CD45^+CD11b^+Ly\text{-}6C^{int}Ly6G^+$), DCs ($CD45^+CD11c^+I\text{-}A/E^{high}$), macrophages ($CD45^+CD11b^+Ly\text{-}6C^-Ly6G^-CD64^+$), γδ T cells ($CD45^+CD3e^+TCR\gamma\delta^+$).

For intracytoplasmic cytokine staining, cells were stimulated with phorbol myristate acetate (50 ng ml^{-1}) and ionomycin (1 μg ml^{-1}). Permeabilized cells were then stained with antibodies against IL-2 (JES6-5H4), TNF (MP6-XT22) and IFNγ (XMG1.2). For FOXP3, EOMES (W17001A), TBET (4B10), HELIOS (22F6), Ki-67 (16A8), granzyme B (2C5/F5) and perforin (S16009A) staining were performed using the FoxP3/Transcription Factor Staining Buffer Set (eBioscience). To assess OVA-specific $CD8^+$ cells, TILs were stained with $H\text{-}2^{Kb}\text{-}OVA_{257–264}$ dextramers (Immudex) and then stained with surface antibodies. To determine TCF1 protein levels, TILs were stained with surface antibodies then fixed and permeabilized with eBioscience Transcription Factor Staining Buffer Set. Cells were then stained with anti-TCF1 antibodies (C63D9) followed by fluorescently tagged anti-rabbit IgG (Cell Signaling). All data were collected on the BD Symphony A5 (BD Biosciences) system and analysed using FlowJo (Tree Star).

In vitro B cell cultures

FACS-sorted total B cells from $Cd19^{cre/+}$, $Havcr1^{BKO}$ mice or TIM-1^+ and TIM-1^- B cells from C57Bl/6J mice were labelled with 5 μM CTV and plated in 96-well U-bottom plates in the presence or absence of LPS (5 μg ml^{-1}, InvivoGen), F(ab')2 fragment donkey anti-mouse IgM (anti-IgM) (10 μg ml^{-1}, Jackson ImmunoResearch) and/or anti-CD40 antibodies (5 μg ml^{-1}, BioLegend) for 72 h in complete medium with or without addition of IFNβ, IFNγ or IFNλ (10 ng ml^{-1}, R&D systems). Cells were then analysed by flow cytometry.

Antibodies and humoral response analysis

Serum immunoglobulin levels were measured using the LEGENDplex Mouse Immunoglobulin Isotyping Panel according to the manufacturer's protocol (BioLegend). For the B16F10-specific antibody assay, sera from naive or B16F10-bearing mice were obtained after intracardiac blood collection. B16F10 and MC38 cell lines were incubated with purified anti-CD16/32 antibodies. Cells were incubated with or without sera and then stained with Alexa Fluor 647-conjugated goat anti-mouse κ (GAM) from Invitrogen to reveal B16F10-specific antibodies. Data are expressed using the mean fluorescent intensity ratio between serum + GAM and GAM alone. Circulating immune complexes were analysed using the circulating immune complex Ig's (total (A+G+M) ELISA kit (Alpha Diagnostic International) according to the manufacturer's instructions.

In vitro B cell–T cell co-culture assays

For antigen presentation assays, LNs and spleens from $Cd19^{cre/+}$ or $Havcr1^{BKO}$ mice were dissociated into single-cell suspensions, as

described above, pulsed with $OVA_{323–339}$ (10 μg ml^{-1}) and sorted by FACS for $CD19^+$ B cells, and then co-cultured with CTV-labelled OT-II T cells at different ratios in a 96-well V-bottom plate. After 4 days, cells were analysed by flow cytometry.

In vivo OT II transfer

$CD45.1^+$ OT II cells were isolated from LNs and spleens of CD45.1 OT II mice and transferred i.v. into CD45.2 $Cd19^{cre/+}$ or $Havcr1^{BKO}$ mice 1 day before s.c. injection of 5×10^5 B16-OVA cells. Tumour growth was monitored and on day 16, OT II cells isolated from TILs and dLNs were analysed by flow cytometry.

Human B cell cultures and analysis

Human peripheral blood mononuclear cells (PBMCs) were isolated using density-gradient centrifugation from whole blood drawn from healthy volunteers. PBMCs were labelled with 5 μM CellTrace Violet (CTV) and plated in 96-well U-bottom plates in the presence of F(ab′)2 fragment donkey anti-human IgM (anti-IgM) (5 μg ml^{-1}, Jackson ImmunoResearch) with anti-CD40 antibodies (1 μg ml^{-1}, Peprotech) for 7 days in X-vivo medium. For some experiments, PBMCs were stimulated in the presence of recombinant IFNβ, IFNγ or IFNλ (all 20 μg ml^{-1}, Peprotech) as indicated. Cells were then analysed by flow cytometry. In brief, Human PBMCs were analysed using the following reagents. Live/dead cell discrimination was performed using the Live/Dead Fixable viability dye 455UV (Thermo Fisher Scientific). For surface staining, the following antibodies were used: CD19 (SJ25C1), CD27 (M-T271), CD38 (HB7), CD86 (IT2.2), IgD (IA6-2) and Tim-1 (1D12) were used. All data were collected on the BD Symphony A5 (BD Biosciences) system and analysed using FlowJo (Tree Star).

Statistics and reproducibility

Unless otherwise specified, each experiment was repeated independently at least twice and all statistical analyses were performed using two-tailed Student's *t*-tests, Mann–Whitney *U*-tests or one-way ANOVA followed by Tukey's multiple-comparison test, using GraphPad Prism (v.8.0). $P < 0.05$ was considered to be significant; $^*P < 0.05$, $^{**}P < 0.01$, $^{***}P < 0.001$, $^{****}P < 0.0001$, unless otherwise indicated.

Reporting summary

Further information on research design is available in the Nature Portfolio Reporting Summary linked to this article.

Data availability

All genomics data produced for this study have been deposited at the GEO under accession number GSE225717. All other data needed to evaluate the conclusions in this paper are available in the Article and its Supplementary Information. Source data are provided with this paper.

53. Khalil, A. M., Cambier, J. C. & Shlomchik, M. J. B cell receptor signal transduction in the GC is short-circuited by high phosphatase activity. *Science* **336**, 1178–1181 (2012).
54. Engblom, C. et al. Osteoblasts remotely supply lung tumors with cancer-promoting $SiglecF^{high}$ neutrophils. *Science* https://doi.org/10.1126/science.aal5081 (2017).
55. Chihara, N. et al. Induction and transcriptional regulation of the co-inhibitory gene module in T cells. *Nature* **558**, 454–459 (2018).
56. Li, B. et al. Cumulus provides cloud-based data analysis for large-scale single-cell and single-nucleus RNA-seq. *Nat. Methods* **17**, 793–798 (2020).
57. Fleming, S. J. et al. Unsupervised removal of systematic background noise from droplet-based single-cell experiments using CellBender. Preprint at *bioRxiv* https://doi.org/10.1101/791699 (2022).
58. Wolock, S. L., Lopez, R. & Klein, A. M. Scrublet: computational identification of cell doublets in single-cell transcriptomic data. *Cell Syst.* **8**, 281–291 (2019).
59. Korsunsky, I. et al. Fast, sensitive and accurate integration of single-cell data with Harmony. *Nat. Methods* **16**, 1289–1296 (2019).
60. Jerby-Arnon, L. & Ruppin, E. Moving ahead on harnessing synthetic lethality to fight cancer. *Mol. Cell. Oncol.* **2**, e977150 (2015).
61. Jerby-Arnon, L. et al. Predicting cancer-specific vulnerability via data-driven detection of synthetic lethality. *Cell* **158**, 1199–1209 (2014).
62. Liu, D. et al. Integrative molecular and clinical modeling of clinical outcomes to PD1 blockade in patients with metastatic melanoma. *Nat. Med.* **25**, 1916–1927 (2019).
63. Lee, J. S. et al. Harnessing synthetic lethality to predict the response to cancer treatment. *Nat. Commun.* **9**, 2546 (2018).
64. Picelli, S. et al. Full-length RNA-seq from single cells using Smart-seq2. *Nat. Protoc.* **9**, 171–181 (2014).
65. Satija, R., Farrell, J. A., Gennert, D., Schier, A. F. & Regev, A. Spatial reconstruction of single-cell gene expression data. *Nat. Biotechnol.* **33**, 495–502 (2015).
66. Afgan, E. et al. The Galaxy platform for accessible, reproducible and collaborative biomedical analyses: 2018 update. *Nucleic Acids Res.* **46**, W537–W544 (2018).
67. Li, B. & Dewey, C. N. RSEM: accurate transcript quantification from RNA-seq data with or without a reference genome. *BMC Bioinformatics* **12**, 323 (2011).
68. Mahoney, K. M. et al. A secreted PD-L1 splice variant that covalently dimerizes and mediates immunosuppression. *Cancer Immunol. Immunother.* **68**, 421–432 (2019).
69. Ye, C. J. et al. Genetic analysis of isoform usage in the human anti-viral response reveals influenza-specific regulation of *ERAP2* transcripts under balancing selection. *Genome Res.* **28**, 1812–1825 (2018).
70. Dann, E., Henderson, N. C., Teichmann, S. A., Morgan, M. D. & Marioni, J. C. Differential abundance testing on single-cell data using *k*-nearest neighbor graphs. *Nat. Biotechnol.* **40**, 245–253 (2022).
71. Tang, Z., Kang, B., Li, C., Chen, T. & Zhang, Z. GEPIA2: an enhanced web server for large-scale expression profiling and interactive analysis. *Nucleic Acids Res.* **47**, W556–W560 (2019).

Acknowledgements We thank all of the members of the Kuchroo laboratory; A. C. Anderson, S. H. Krovi, A. Kohl and M. Collins for discussions; J. Xia, H. Stroh, D. Kozoriz and R. Kumar for laboratory support; and C. Lambden for computational advice. The work was supported by the grants Melanoma Research Alliance (MRA; 926682); P01AI129880, P01AI039671, P01AI073748, P01AI056299 and R01AI144166 from the National Institutes of Health (to V.K.K.); by the Klarman Cell Observatory and HHMI (to A.R.). Y.-C.K. was supported by the NMSS FG-2007-36929; L.B. by the Philippe Foundation; and L.A. by the LabEx MAbImprove (ANR-10-LABX-53-01).

Author contributions L.B. and V.K.K. conceived the study. L.B., with assistance from Y.-C.K., J.S., A.S., S.M.O., M.Y.V.-F., D.E.F., J.F., R.M.B., S.Z. and S.X., designed, performed and analysed the biological experiments. L.B., with assistance from Y.-C.K., J.S., A.S., E.C. and T.M.D., performed the sequencing experiments with guidance from A.R. and O.R.-R. L.B., N.S., C.J.G., Z.L., F.J.Q., O.A. and E.T.T. designed and performed the computational analysis with guidance from A.R. L.B., J.S., E.T.T., L.A., V.K.K. and A.R. interpreted the results. J.R.K. and A.H.S. generated and provided the $Pdcd1^{fl/fl}$ mice. K.M. and D.M.R. generated and performed the experiments using the $Cd19^{cre/+} \times Il10^{fl/fl}$ mice. The manuscript was written by L.B. with assistance from E.T.T. and was edited by L.A., A.R. and V.K.K. with input from all of the authors.

Competing interests V.K.K. has an ownership interest in and is a member of the scientific advisory board for Tizona Therapeutics, Bicara Therapeutics, Compass Therapeutics, Larkspur Biosciences and Trishula Therapeutics. L.B., S.X. and V.K.K. are named as inventors on a provisional patent that has been filed including work from this study. L.A. performed consultancy work for Roche, Merck, Bristol-Myers Squibb and Orega Biotech, and was a recipient of a research grant from Sanofi. A.R. and V.K.K. are co-founders of and have an ownership interest in Celsius Therapeutics. A.R. is also a co-founder and equity holder in Immunitas Therapeutics and was a scientific advisory board member of Thermo Fisher Scientific, Syros Pharmaceuticals, Asimov and Neogene Therapeutics until 31 July 2020. A.R. and O.R.-R. are listed as co-inventors on patent applications filed by the Broad Institute to inventions relating to single-cell genomics. The interests of V.K.K. were reviewed and managed by the Brigham and Women's Hospital and Partners Healthcare in accordance with their conflict-of-interest policies. The interests of A.R. were reviewed and managed by the Broad Institute and HHMI in accordance with their conflict-of-interest policies. Since 1 August 2020, A.R. has been an employee of Genentech, a member of the Roche group. O.R.-R. is currently an employee of Genentech. The other authors declare no competing interests.

Additional information

Supplementary information The online version contains supplementary material available at https://doi.org/10.1038/s41586-023-06231-0.

Correspondence and requests for materials should be addressed to Aviv Regev or Vijay K. Kuchroo.

Peer review information *Nature* thanks Menna Clatworthy and the other, anonymous, reviewer(s) for their contribution to the peer review of this work.

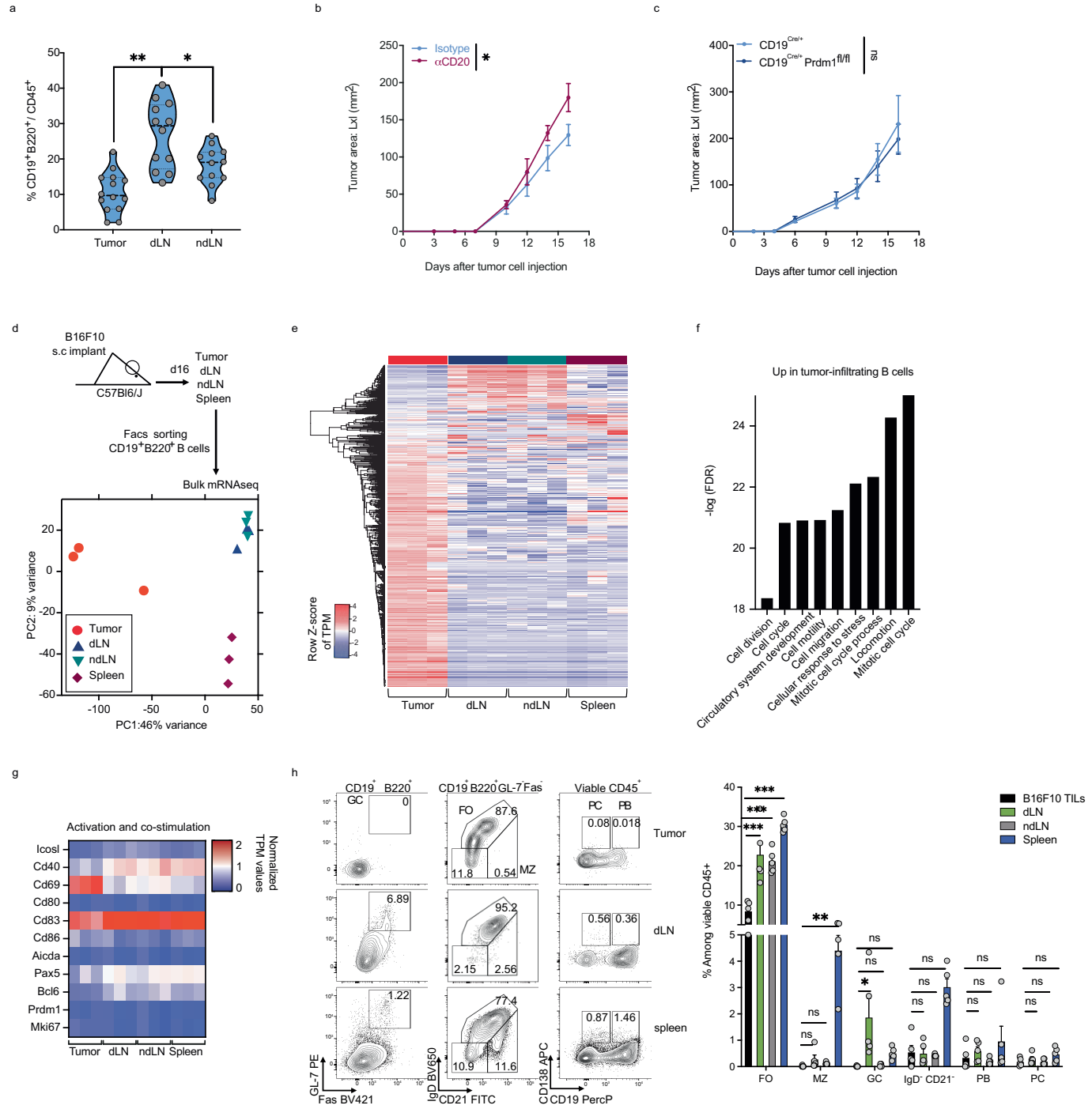

Extended Data Fig. 1 | Total B cells but not plasma cells limit tumour growth and B16F10-infiltrating B cells have a distinct phenotype. a, Frequencies of B cells among CD45$^+$ cells derived from tumour, dLN, ndLN from C57Bl6/J mice 16 days post tumour implantation. **b**,**c**, B16F10 tumour growth in C57Bl/6J treated with anti-CD20 (48h prior to tumour injections) or isotype control antibodies (n = 5 mice per group) (**b**) or CD19$^{Cre/+}$ and CD19$^{Cre/+}$xPrdm1$^{fl/fl}$ (n = 5 mice per group). **d**–**g**, Bulk RNAseq analysis of B cells derived from tumour, dLN, ndLN and spleen of B16F10-bearing wild-type mice (n = 3). Experimental design and PCA plot (**d**), Heatmap of global gene expression (**e**), Pathway enrichment analysis of genes up-regulated in tumour-derived B cells (**f**) and heatmap of a selected set of genes (**g**). **h**, Flow cytometry analysis of B cells derived from tumour, dLN, ndLN and spleen of C57Bl6/J mice implanted with B16F10 *s.c*. Representative FACS plot and percentage of B cell subsets. Heatmap depicting the MFI of various B cell markers in B cells derived from tumours or dLN from C57Bl6/J mice (n = 5) (**h**). Data are mean ± s.e.m and pooled or representative of at least two to three independent experiments. * $p < 0.05$, ** $p < 0.01$, *** $p < 0.0001$. Repeated measures two-way ANOVA test in **b** and **c**. two-tailed Student's t-test in **a**. two-way ANOVA with Tukey's multiple comparisons test in **h**.

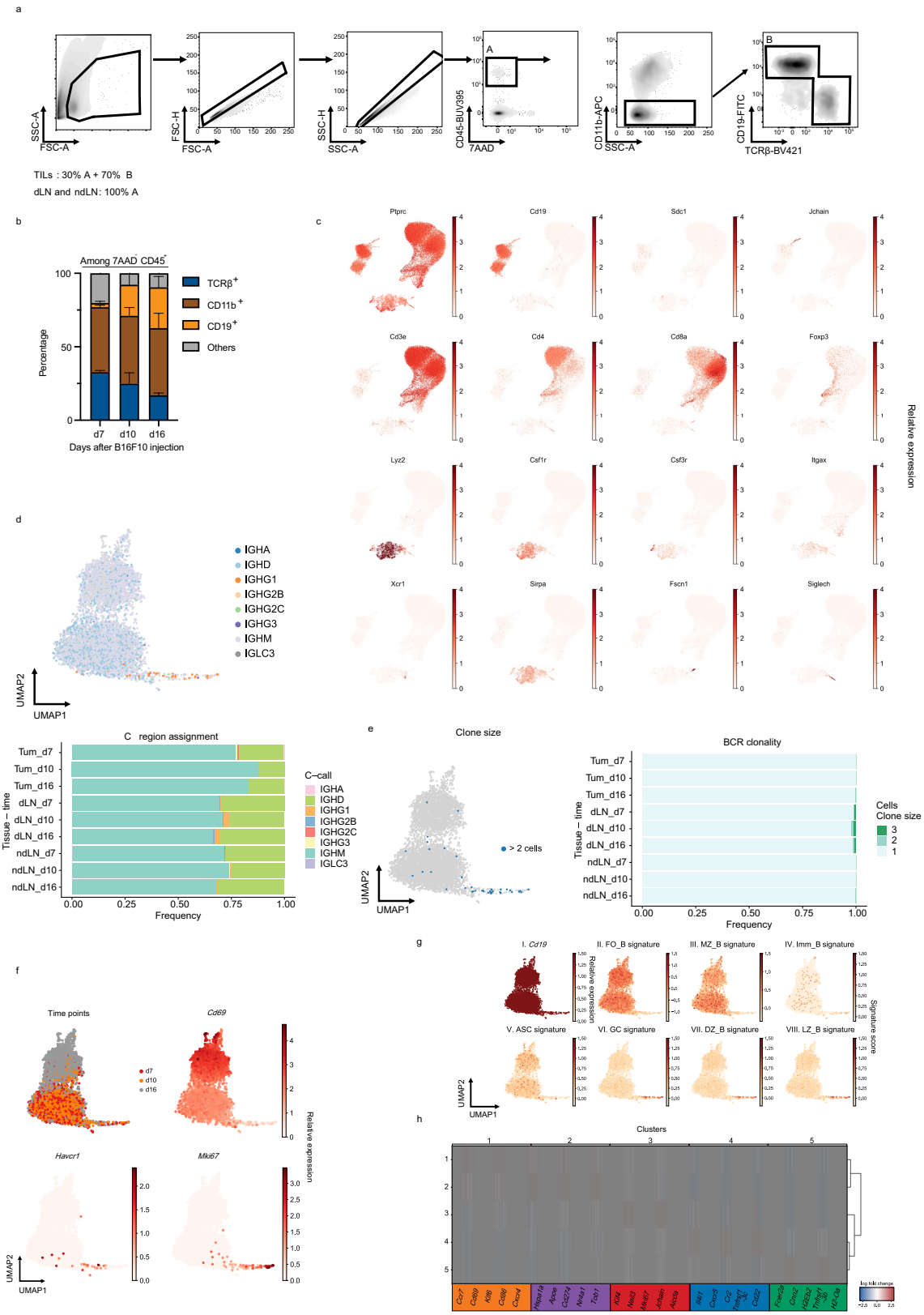

Extended Data Fig. 2 | scRNAseq and BCRseq of TILs, dLN and ndLN derived from B16F10 melanoma bearing mice. a, Gating strategy for the sorting of singlet viable cells prior to scRNAseq. **b**, Flow cytometry analysis depicting proportions of cell types infiltrating tumours across time. Data are mean ± s.e.m from two experiments. n = 3 mice per group. **c**, UMAP of expression of different lineage marker transcripts. **d,e**, UMAPs and quantification of immunoglobulin class-switch (**d**) and clonal expansion (**e**) in B cells. **f** and **g**, UMAPs of B cells coloured by time points or relative expression of the indicated genes (**f**) and **g**, Panels I-VIII, cells are coloured by *Cd19* expression (I) or by their signature score that reflects the relative average expression of the genes overlapping with the signatures for several indicated B cell subsets (II-VIII). Follicular (FO_B), Marginal zone (MZ_B), Immature (Imm_B), Antibody secreting cells (ASC), germinal centre (GC) B cells derived from the dark zone (DZ_B) or light zone (LZ_B). **h**, Heatmap depicting the log fold change of the top 100 genes uniquely up-regulated in each Leiden cluster (t-test; fold change >2). Selected genes are shown.

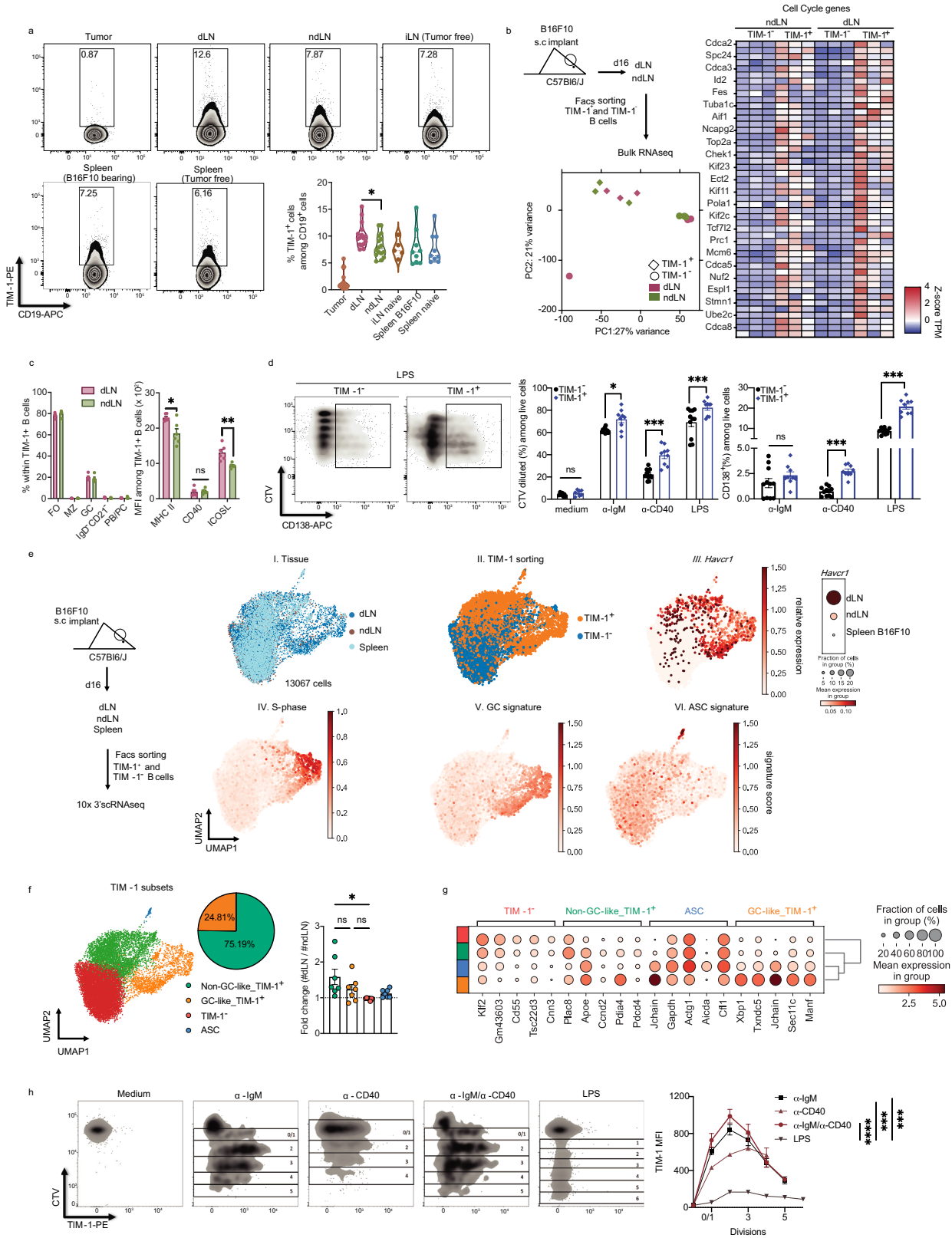

Extended Data Fig. 3 | See next page for caption.

Extended Data Fig. 3 | TIM-1 expressing B cells characterization. **a**, Proportions of TIM-1$^+$ cells among CD19$^+$ cells derived from tumour, dLN, ndLN, and spleen from B16F10 bearing C57Bl6/J mice 16 days post tumour injection together with inguinal LN (iLN) and spleen from tumour-free WT mice (n = 5 for pLN, n = 9 for spleens, n = 16 for Tumour, dLN and ndLN). **b**, TIM-1$^+$ B cells derived from dLN and ndLN were sorted and analysed by bulk RNAseq (n = 3). Experimental design, PCA plot and heatmap of selected genes are shown. **c**, Flow cytometry analysis of subsets and marker expression of TIM-1$^+$ B cells derived from dLN vs ndLN from B16F10-bearing WT mice (n = 6). **d**) FACS-sorted TIM-1$^-$ and TIM-1$^+$ B cells were stained with CTV and stimulated *in vitro* with anti-IgM, anti-CD40 or LPS for 72h. Cell proliferation and plasma cell differentiation was analysed by flow cytometry. Representative FACS plot (left) and quantification (right) are shown (n = 7 for medium, for stimulation n = 11 for TIM-1- and n = 9 for TIM-1+). **e**, **f**, scRNAseq analysis depicting the experimental design, UMAPs coloured by tissue of origin (I), TIM-1 sorting (II), expression of *havcr1* (III) and gene signature score of cell cycle S-phase (IV), germinal centre cells (V) and antibody secreting cells (VI). Dotplot of *Havcr1* expression (III. right). **f**, UMAP coloured by B cell clusters annotated according to TIM-1 expression. Pie chart depicting the frequency of the two main TIM-1-expressing subsets and foldchange of cell numbers between dLN and ndLN for each subset (n = 7). **g**, Top 5 differentially expressed genes (FDR < 0.05 and LFC > 1) (x axis) by cluster (y axis). Dot size represents the fraction of cells in the cluster that express the gene; colour indicates the mean expression (logTP10K (see Methods)) in all cells, relative to other clusters. **h**, FACS-sorted TIM-1$^-$ B cells were stained with CTV and stimulated *in vitro* with LPS, anti-IgM, anti-CD40 (n = 3) or both anti-IgM+anti-CD40 (n = 4) for 72 h. TIM-1 surface expression across cell divisions was analysed by flow cytometry. Representative FACS plot (left) and TIM-1 MFI quantification (right). Flow cytometry data are mean ± s.e.m and pooled or representative of at least two to three independent experiments. * $p < 0.05$, ** $p < 0.01$, *** $p < 0.001$, **** $p < 0.0001$, two-way ANOVA test in **h**. two-tailed Student's t-test in **a,c,d** and **f**.

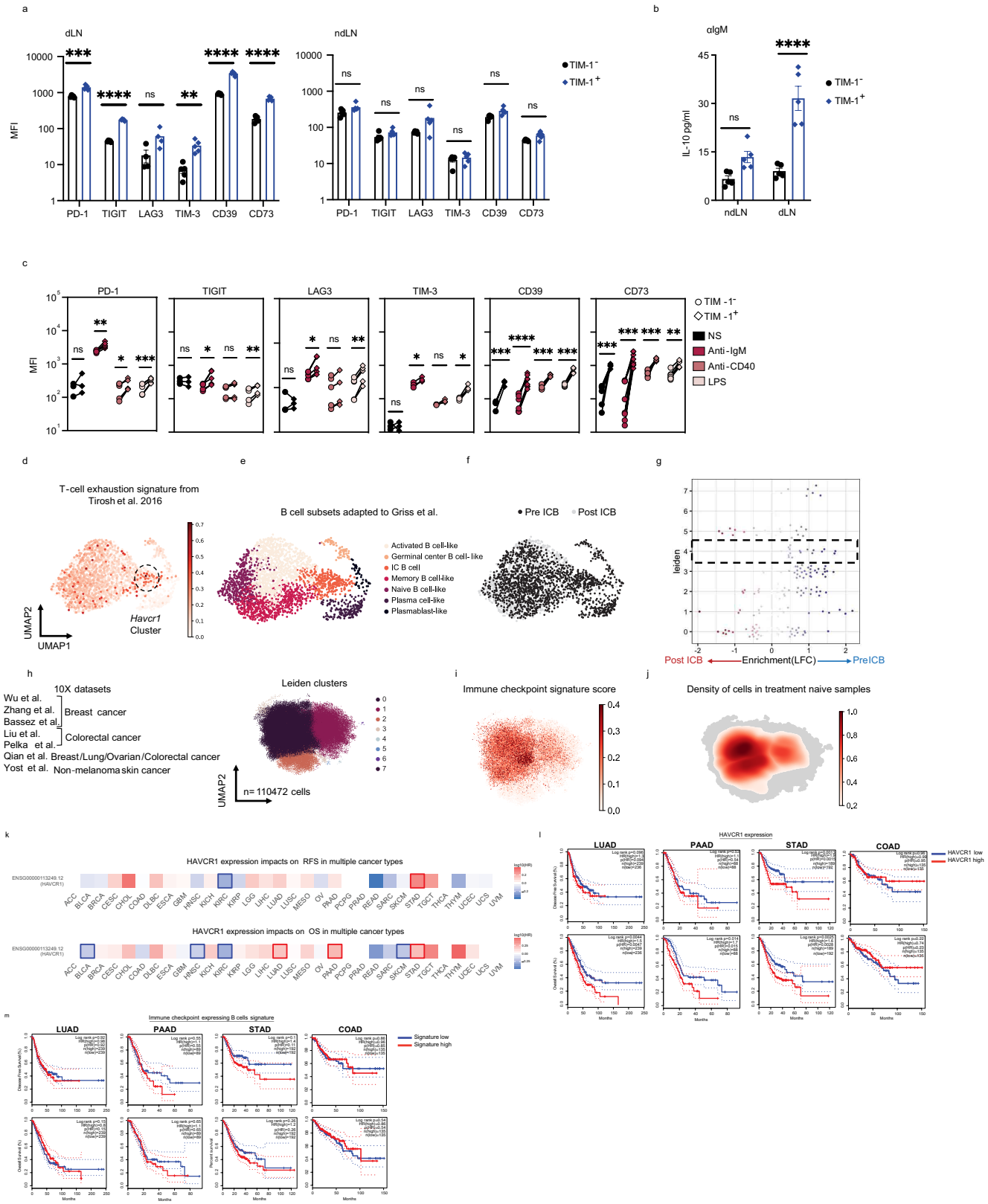

Extended Data Fig. 4 | See next page for caption.

Extended Data Fig. 4 | TIM-1 expressing B cells express higher levels of checkpoint molecules and IL-10. a–**b**, TIM-1$^+$ and TIM-1$^-$ B cells derived from dLN and ndLN from B16F10 bearing C57Bl6/J mice were analysed *ex vivo*. MFI of various checkpoint molecules (n = 4 mice per group) (**a**), IL-10 secretion 24 h post anti-IgM stimulation as determined by LegendPlex (n = 5 mice per group) (**b**). **c**, FACS-sorted TIM-1$^-$ and TIM-1$^+$ B cells were stimulated *in vitro* with anti-IgM, anti-CD40 or LPS for 72 h. MFI of checkpoint molecules was analysed by flow cytometry. **d**–**f**, UMAP plot of published scRNAseq data depicting 2615 B cells(dots) isolated from human tumours, coloured by their signature score that reflects the relative average expression of the genes overlapping with the signature of human melanoma exhausted T cells from Tirosh et al. 2016 (**d**), known B-cell subsets[4] (**e**) or Leiden clusters (**f**). **g**, Beeswarm plots of the distribution of log fold change across Pre and Post ICB treatment from the Merge SS2 datasets using miloR[70]. **h**–**j**) UMAPs depicting each single cell dots coloured by Leiden clusters (**h**), Immune checkpoint signature score (**i**) or density plot for treatment-naive samples (**j**). Flow cytometry data are mean ± s.e.m and pooled or representative of at least two to three independent experiments. **k**, Survival map depicting the association of *HAVCR1* high expression and clinical outcome in 32 cancer types. High log10 Hasard ratio (HR) (Reds) indicates a negative correlation with survival which would be outlined if $p \leq 0.05$. **l** and **m**, Kaplan Meier disease free (top row) or Overall (bottom row) survival curves for TIM-1 expression (**l**) or IC B cells signature (**m**) in Lung (LUAD), pancreatic (PAAD), stomach (STAD) and colon (COAD) adenocarcinomas. For each signature gene set, the cohorts were divided into high and low expression groups by median value (50% cutoff). Analyses were performed with log-rank Mantel-Cox test using web server GEPIA2[71], based on TCGA and GTEx databases. * $p < 0.05$, ** $p < 0.01$, *** $p < 0.001$, **** $p < 0.0001$, paired two-tailed t-test in **a**,**b**, and **c**.

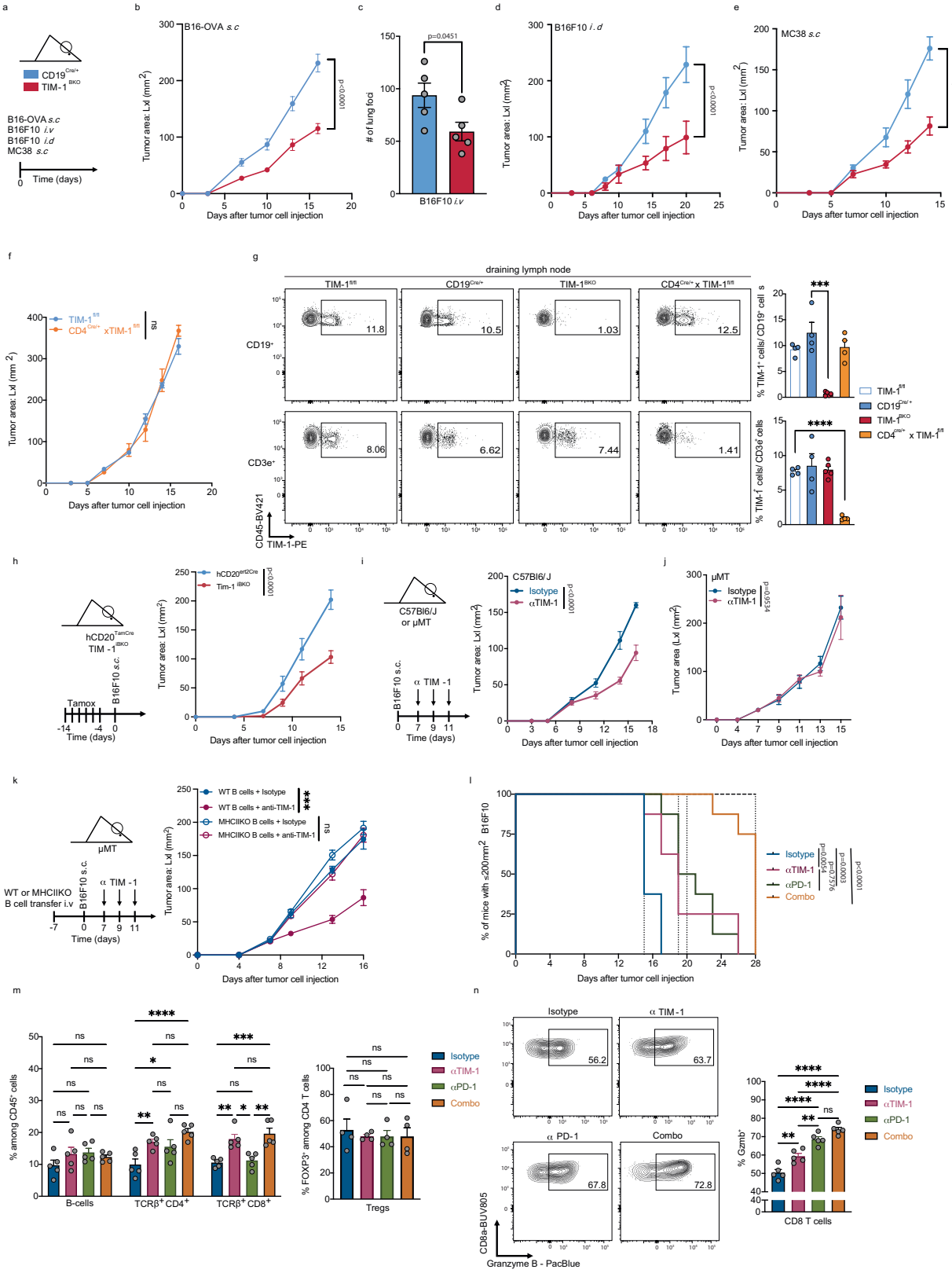

Extended Data Fig. 5 | See next page for caption.

Extended Data Fig. 5 | TIM-1 loss in B cells but not T cells limits tumor growth and anti-TIM-1 treatment requires MHC II expression on B cells. a–**e**, Tumour growth in $CD19^{Cre/+}$ and $TIM\text{-}1^{BKO}$ mice implanted with B16-OVA (n = 5 control vs 5 $TIM\text{-}1^{BKO}$) (**b**), intravenously (n = 5 control vs 5 $TIM\text{-}1^{BKO}$) (**c**), intradermally (n = 4 control vs 5 $TIM\text{-}1^{BKO}$) (**d**) or subcutaneous MC38 colon adenocarcinoma (n = 6 control vs 6 $TIM\text{-}1^{BKO}$) (**e**). **f**, Tumour growth curve of B16F10 implanted into $TIM\text{-}1^{fl/fl}$ and $CD4^{Cre/+}$x$TIM\text{-}1^{fl/fl}$ mice (n = 4). **g**, Subcutaneous B16F10 melanoma were subcutaneously implanted into $CD19^{Cre/+}$, $TIM\text{-}1^{BKO}$, $TIM\text{-}1^{fl/fl}$ and $CD4^{Cre/WT}$ x$TIM\text{-}1^{fl/fl}$ mice. On day 16 dLN were harvested followed by flow cytometric analysis of TIM-1 expression of $CD19^{+}$ or $CD3e^{+}$ cells. n = 4 mice per group. **h**, B16F10 melanoma growth in $TIM\text{-}1^{iBKO}$ and $hCD20^{ert2Cre}$ mice treated with tamoxifen on days indicated prior to tumour inoculation (n = 6 mice per group). **i**–**k**, B16F10 tumour growth with anti-isotype control or anti-TIM-1 treatment in C57Bl/6J (n = 7 treated with isotype control vs n = 9 treated with anti-TIM-1), μMT (n = 5 per group) (**j**) or μMT mice were reconstituted with WT or MHCII KO B cells and treated with anti-TIM-1 antibody (n = 5 mice per group) (**k**). Experimental design (**k, left**), tumour growth curves (**k, right**). **l**–**n**, Survival curves (**l**) and flow cytometry immunophenotyping of TILs depicting frequencies of B cells, CD4+ and CD8+ TILs among living $CD45^{+}$ cells (**m, left**), FOXP3+ cells among CD4+ TILs (**m, right**) and granzyme B^{+} cells among CD8+ TILs (**n**) of C57Bl/6J implanted with B16F10 melanoma and treated with either anti-TIM-1, anti-PD-1, anti-TIM-1 + anti-PD-1 (combo), or isotype controls (n = 8 mice per group for tumour growth analysis and 5 mice per group for flow cytometry analysis). Data are mean ± s.e.m and pooled from two to three independent experiments. * $p < 0.05$, ** $p < 0.01$, *** $p < 0.001$, **** $p < 0.0001$. Repeated measures two-way ANOVA test in **b,d,e,f,h,l,j** and **k**. unpaired two-tailed t-test in **c** and **g**. Differences between survival curves were analysed by log-rank (Mantel–Cox) test (**l**). One or two-way ANOVA with Tukey's multiple comparisons test in **m** and **n**.

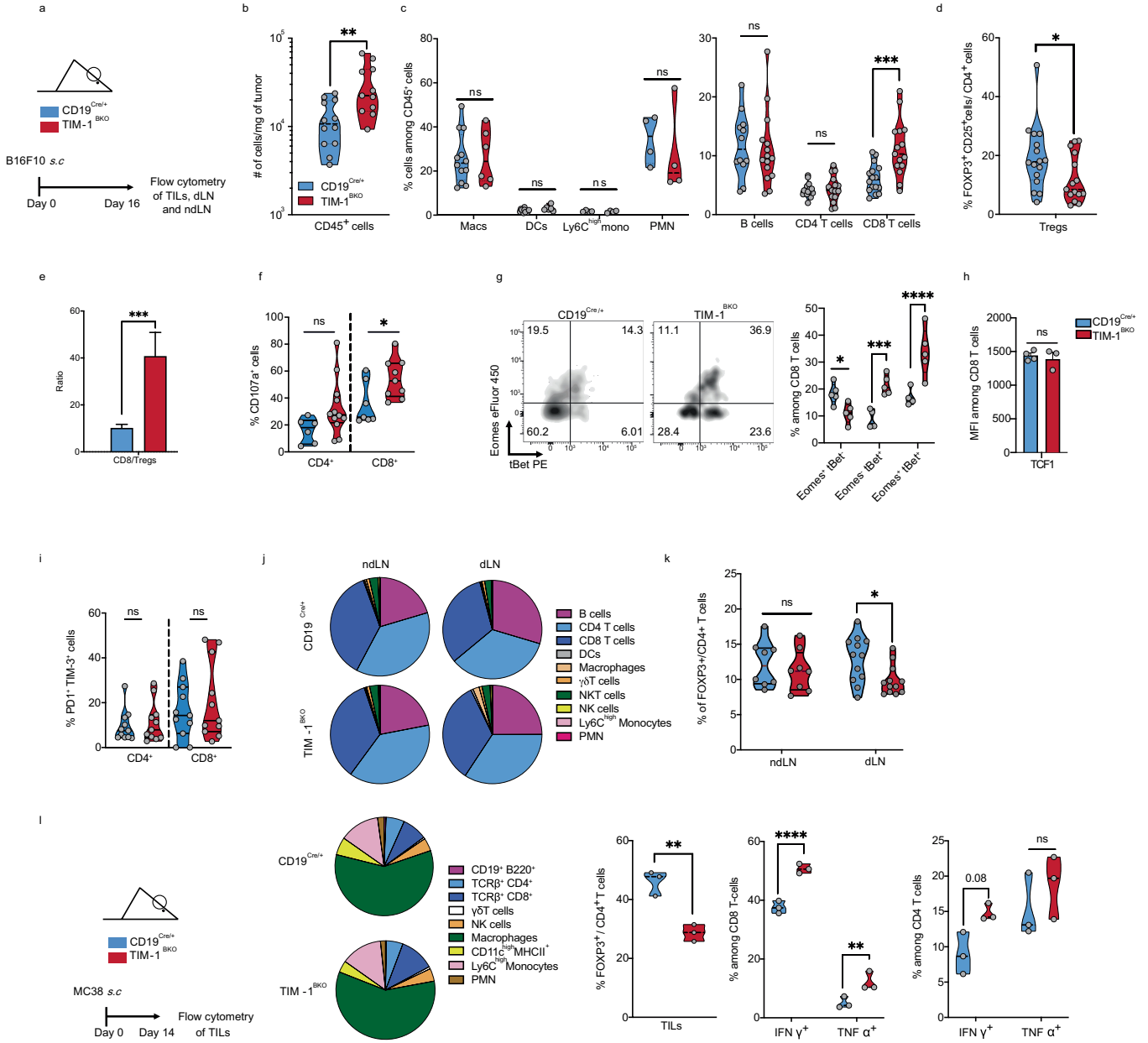

Extended Data Fig. 6 | Immunophenotyping of tumour-bearing CD19$^{Cre/+}$ and Havcr1/TIM-1^{BKO} mice. a–k, Flow cytometry analysis of TILs, dLN and ndLN derived from CD19$^{Cre/+}$ and TIM-1^{BKO} mice implanted with B16F10 *s.c*. Absolute number of live CD45$^+$ cells per gram of tumour (n = 12 controls and n = 11 TIM-1^{BKO} mice) (**b**), Macs, DCs (n = 12 controls and n = 6 TIM-1^{BKO} mice), mono, PMN (n = 4 controls and n = 4 TIM-1^{BKO} mice), B cells (n = 12 controls and n = 15 TIM-1^{BKO} mice), CD4+ and CD8+ T cells frequencies among CD45$^+$ cells (n = 16 controls and n = 15 TIM-1^{BKO} mice) (**c**), Frequency of Tregs among CD4+ T cells (n = 16 mice per group) (**d**), CD8+ T cells *vs* Tregs ratio (**e**). CD107a-expressing *CD4*+(n = 6 controls and n = 12 TIM-1^{BKO} mice) and CD8+ T cells (n = 7 controls and n = 9 TIM-1^{BKO} mice) (**f**), Eomes and/or Tbet fraction (n = 5 mice per group) (**g**), MFI of TCF1 (n = 4 controls and n = 3 TIM-1^{BKO} mice) (**h**) and Frequency PD-1$^+$ TIM-3$^+$ among CD8+ T cells (**d**). **j**, pie charts depicting the proportions of various immune cell populations with dLN and ndLN. **k**, frequencies of FOXP3$^+$ cells among CD4+ T cells (n = 8 mice per group). **l**, Flow cytometry analysis of TILs from derived from CD19$^{Cre/+}$ and TIM-1^{BKO} mice implanted with MC38 colon adenocarcinoma *s.c*. Experimental design, pie chart of immune population and frequencies of FOXP3$^+$ CD4+ T cells and of IFNγ or TNFα expressing CD8+ and CD4+ T cells (n = 4 mice per group). Data are mean ± s.e.m and pooled from two to three independent experiments. * p < 0.05, ** p < 0.01, *** p < 0.001, **** p < 0.0001, two-tailed Student's t-test in **b,c,d,e,f,g,h,i,k** and **l**.

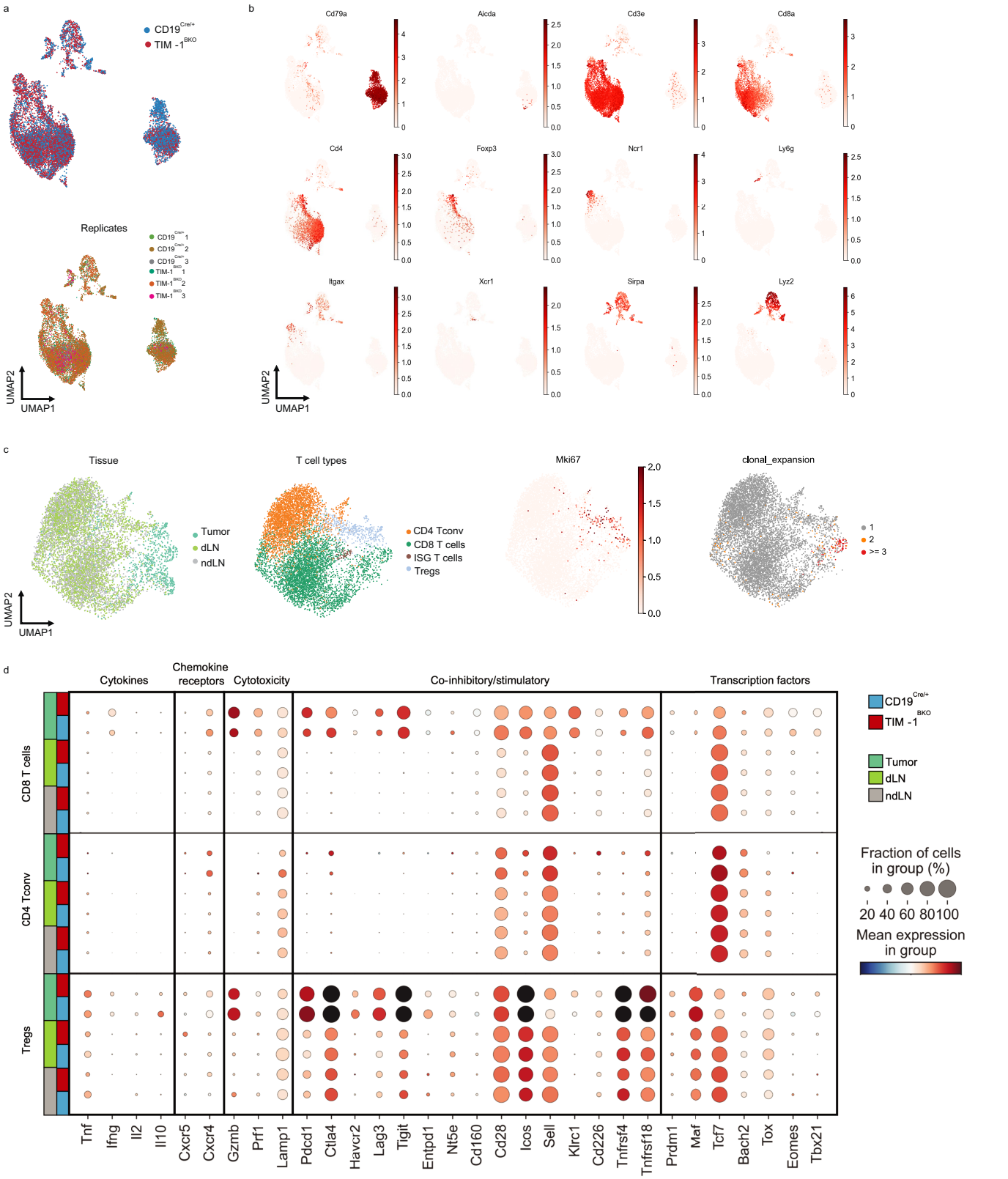

Extended Data Fig. 7 | scRNAseq of TILs, dLN and ndLN derived from B16F10 bearing CD19$^{Cre/+}$ and Havcr1/TIM-1^{BKO} mice. a,b, scRNA/TCR-seq of TILs, dLN and ndLN from CD19$^{Cre/+}$ and TIM-1^{BKO} mice bearing B16F10 melanoma. UMAPs coloured by genotype (**a, top**), biological replicates (**a, bottom**) or the relative expression of the indicated genes (**b**). **c**, UMAPs of T cells coloured by tissue, T cell types, *Mki67* relative expression or clonal expansion as indicated. **d**, Gene expression for functional marker genes in T cells. For each gene (columns) in each group (rows), the proportion of cells in the group expressing the gene (dot size) and the relative mean expression of expressing cells (colour) is plotted.

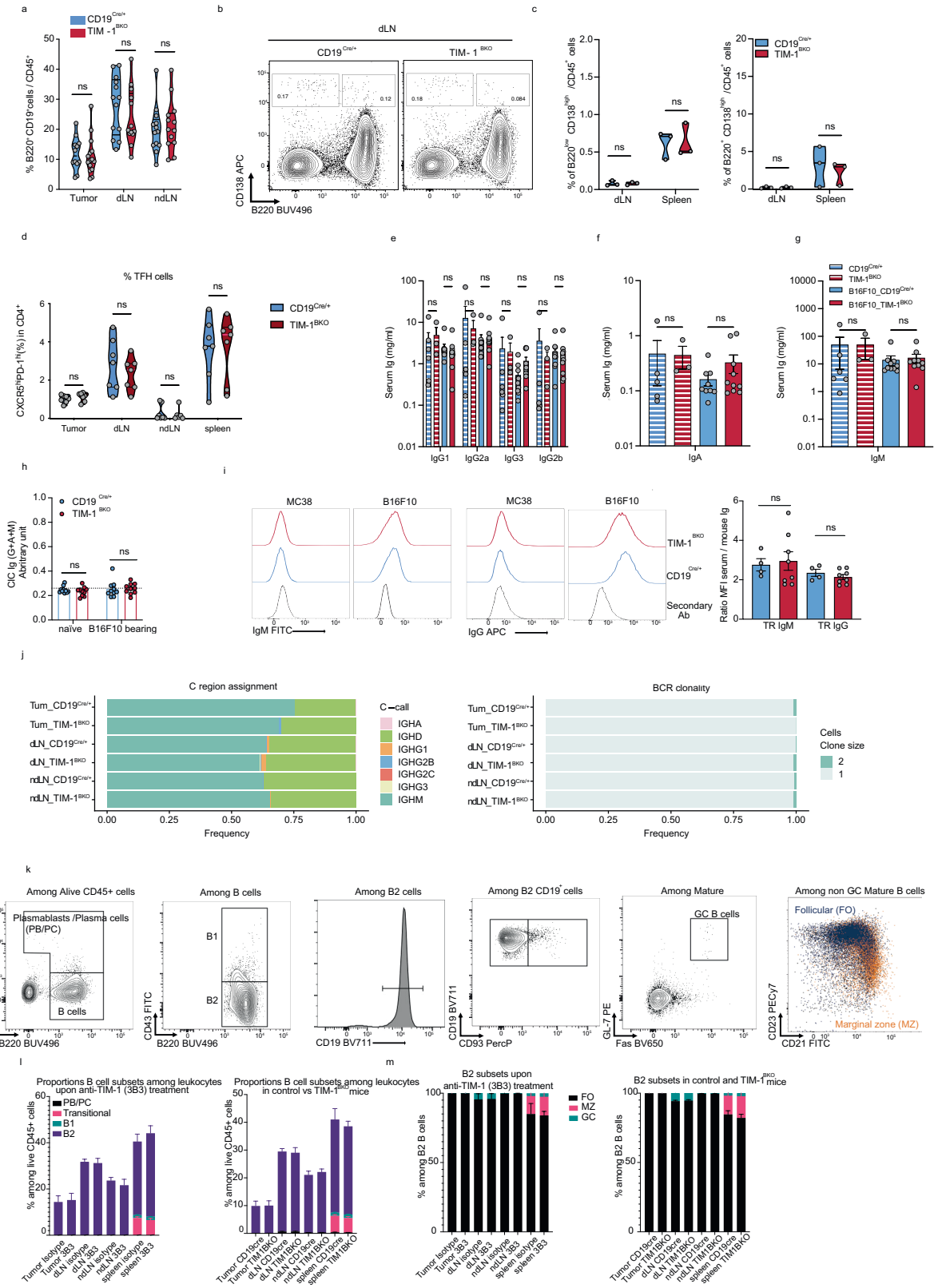

Extended Data Fig. 8 | See next page for caption.

Extended Data Fig. 8 | Analysis of the humoral immunity and B-cell subsets in B16F10 bearing CD19$^{Cre/+}$ and Havcr1/TIM-1^{BKO} mice. a, Frequencies of B cells among CD45^{+} TILs derived from CD19$^{Cre/+}$ and TIM-1^{BKO} mice implanted with B16F10 *s.c*. **b,c**, Representative FACS plot (**b**) and percentage (**c**) of plasma cells (B220^{low} CD138^{high}) or plasmablasts (B220^{+} CD138^{high}) or TFh cells (**d**) from CD19$^{Cre/+}$ and TIM-1^{BKO} mice implanted with B16F10 *s.c*. **e**–**h**, serum immunoglobulins or CICs from naive (n = 5 CD19$^{Cre/+}$ and n = 3 TIM-1^{BKO}) or B16F10-bearing CD19$^{Cre/+}$ and TIM-1^{BKO} mice (n = 9 per group) and measured by LegendPlex (**e**–**g**) or ELISA (**h**). **i**, Flow-cytometric analysis of the presence of antitumor antibodies in the sera of CD19$^{Cre/+}$ and TIM-1^{BKO} mice implanted with B16F10 *s.c*. Representative histograms (light grey, staining with the secondary antibody alone; blue, CD19$^{Cre/+}$ mice serum (n = 4); red, TIM-1^{BKO} mice serum (n = 8)), and MFI ratios were calculated by dividing the MFI obtained with a given serum by the MFI obtained with the secondary antibody. **j**, Quantification of Immunoglobulin class-switch (**left**) and BCR clonality (**right**) in CD19$^{Cre/+}$ and TIM-1^{BKO} B cells. **k**–**m**, Flow cytometry analysis of B cell subsets in Tumour, dLN, ndLN and spleen from isotype vs anti-TIM-1 (3B3) treatment mice or in control vs TIM-1^{BKO} mice (n = 5 mice per group). **k**, Gating strategy used. **l** and **m**, Bar plots depicting the frequencies of major B-cell subsets (**l**) or subsets within B2 cells (n = 5 mice per group) (**m**). Data are mean ± s.e.m and pooled from two to three independent experiments. Two-tailed Student's t-test in **a,c,d,h** and **i**. two-way ANOVA with Tukey's multiple comparisons test in **e,f,g**.

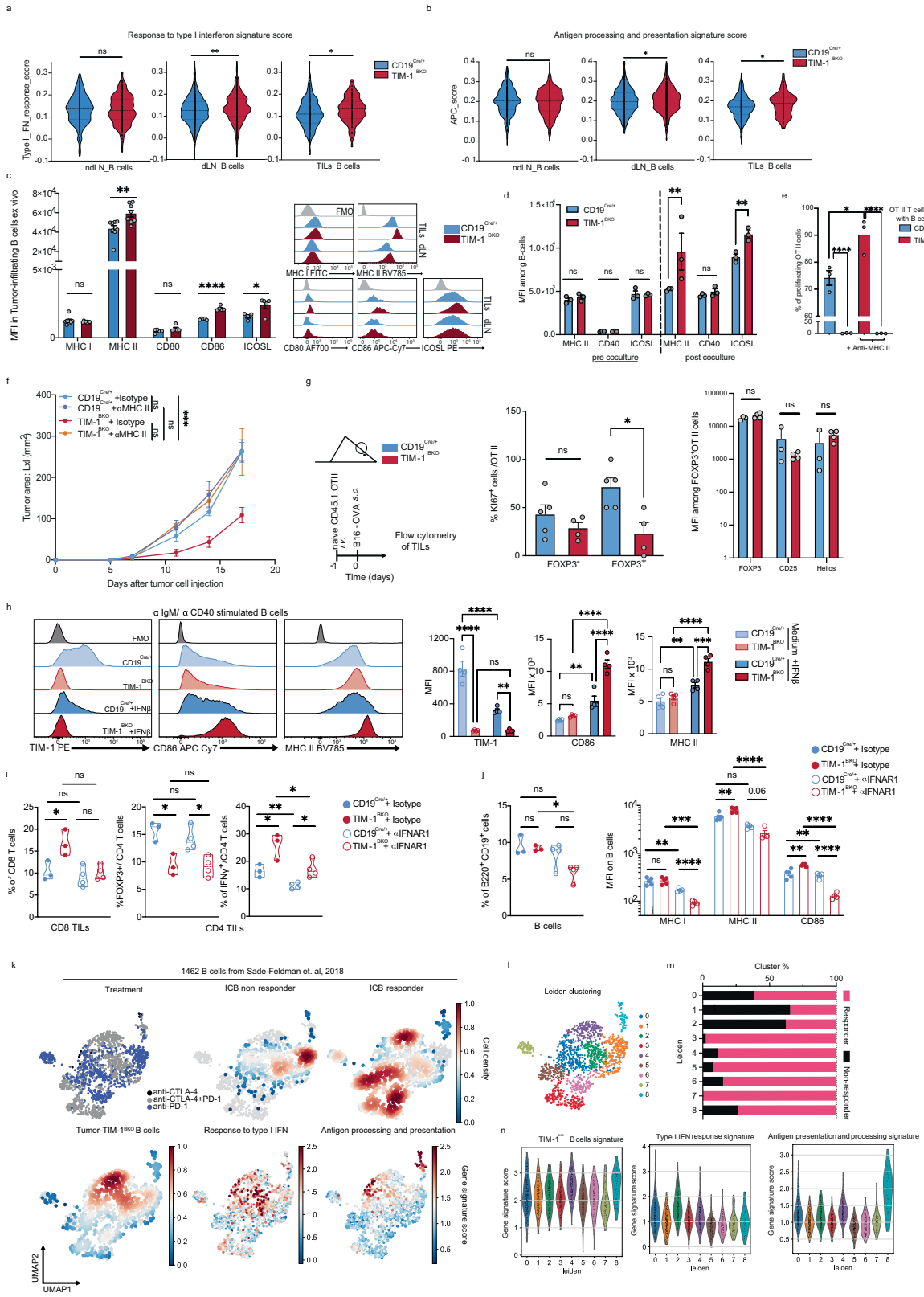

Extended Data Fig. 9 | See next page for caption.

Extended Data Fig. 9 | Havcr1/TIM-1^{BKO} B cells exhibit enhanced antigen presentation and co-stimulation capacity. a and **b**, Violin plots displaying the distribution of the type I interferon response signature score (**a**) or the antigen processing and presentation of peptide antigen (APC) signature score (**b**) between TIM-1^{BKO} and CD19$^{Cre/+}$ B cells derived from ndLN, dLN and TILs. **c** and **d**, MFI and histograms of MHC I and II as well as co-stimulation molecules *ex vivo* (n = 8 mice per group) (**c**) or *in vitro* co-cultured with OT II CD4+ T cells (n = 3) (**d**). **d** and **e**, $OVA_{323-339}$ peptide-pulsed TIM-1^{BKO} and CD19$^{Cre/+}$ B cells were co-cultured with CTV-labelled OVA-restricted CD4+ T cells for 4 days with or without anti-MHC II antibody. T cell proliferation was determined by dilution of CTV. Quantitative analysis of proliferation indices is shown (**e**). **f**, B16F10 melanoma growth in CD19$^{Cre/+}$ and TIM-1^{BKO} mice treated with anti-MHC II or isotype control antibodies (n = 5 mice per group). **g**, Naive CD45.1^{+} OVA-restricted CD4+ T cells were transferred *i.v.* 1 day prior to B16-OVA melanoma cells *s.c* implantation into CD45.2^{+} CD19$^{Cre/+}$ and TIM-1^{BKO} mice (n = 5 mice per group). Tumour-infiltrating OT II cells were examined for expression of KI67 as proportions of expressing cells or MFI of FOXP3, CD25 and Helios (n = 3 CD19$^{Cre/+}$ and n = 4 TIM-1^{BKO} mice). Schematic of the experimental and quantitative results are depicted. **h**, TIM-1^{BKO} and CD19$^{Cre/+}$ B cells cultured with anti-IgM/anti-CD40 for 72 h in the absence (medium) or with 20 ng/ml of IFN-β. Representative histograms (left) and quantitative analysis of the MFI of TIM-1, CD86 and MHC II (n = 4 mice per group). **i** and **j**, Flow cytometry analysis of TILs of indicated mice implanted with B16F10 melanoma and treated with isotype control (n = 3 mice per group) or neutralizing anti-IFNAR-1 antibody (n = 4 mice per group). Frequencies of CD8+ T cells (**i, left**), FOXP3+ and IFNγ+ cells among CD4+ T cells (**i, middle** and **right**), B cells (**j, left**) and MFI of MHC I, MHC II and CD86 among B cells (**j, right**) are depicted. **k**–**n**, Analysis of published scRNAseq[20] data depicting 1462 B cells (dots) isolated from human melanoma tumours, projected onto UMAPs coloured by treatment group (top left), density of cells associated with responder, non-responder lesions (top middle and right) or signature scores of tumour-derived TIM-1^{BKO} B cells, GO type I interferon response and GO antigen processing and presentation gene signatures as detailed in *Methods*. **l**, UMAP coloured by Leiden cell clusters (resolution 1). **m**, stacked bar graph displaying the frequencies of B cells derived from Responder and Non-responder samples among each Leiden cluster and **n**, violin plots displaying the signature scores of the indicated signatures across clusters. Data are mean ± s.e.m and pooled from two to three independent experiments. * $p < 0.05$, ** $p < 0.01$, *** $p < 0.001$, **** $p < 0.0001$. Kruskal-Wallis test in **a** and **b**. Two-tailed Student's t-test in **c,d,e,g,h,i** and **j**. Repeated measures two-way ANOVA test in **f**.

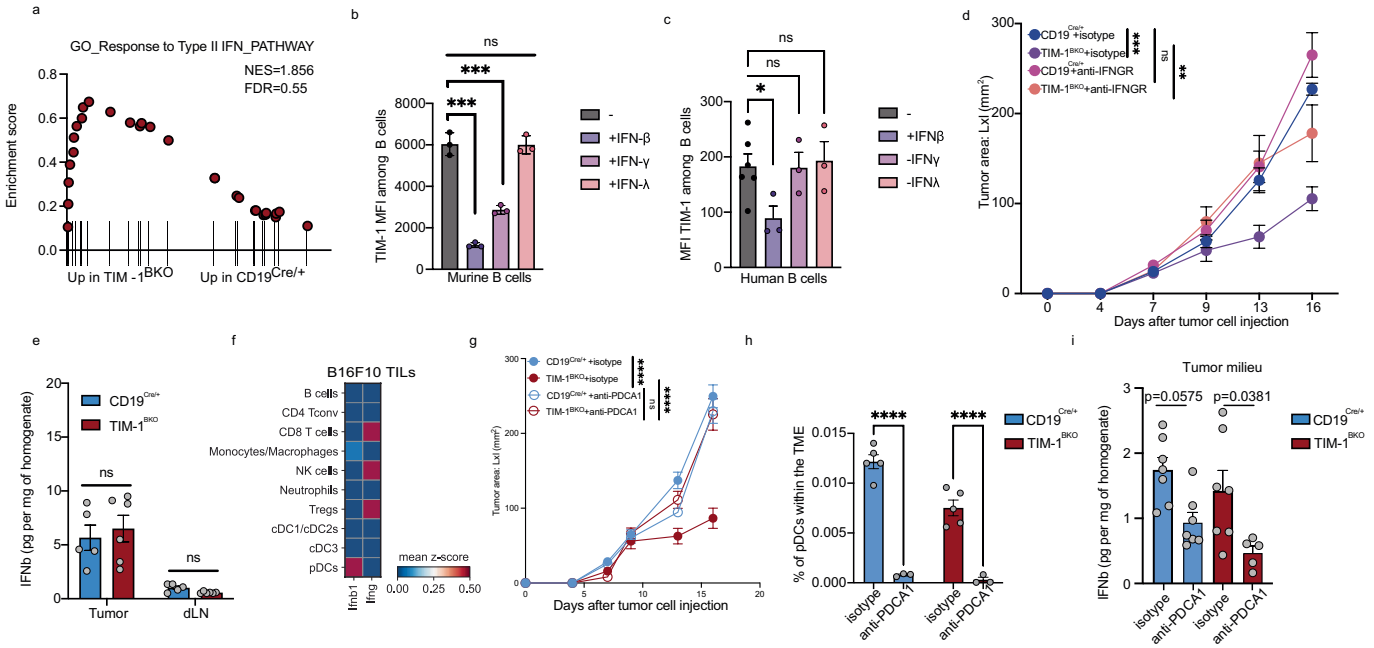

Extended Data Fig. 10 | Source of Interferons in B16F10 tumours and impact on TIM-1-mediated anti-tumour immunity. a) GSEA analysis for the "Response to type II IFN pathway" of tumour-infiltrating TIM-1^{BKO} and CD19$^{Cre/+}$ B cells. **b** and **c**) Murine (b) or human (c) B cells were stimulated with IgM/CD40 for 3 and 7 days respectively in the presence or not of IFNβ, IFNγ or IFNλ (n = 3). TIM-1 expression (MFI) was analysed by flow cytometry. **d**) Tumour growth in indicated mice implanted with B16F10 melanoma and treated with isotype control or neutralizing anti-IFNGR-1 antibody (n = 5 mice per group). **e** and **i**) B16F10 tumour and dLN supernatants derived from CD19$^{Cre/+}$ and TIM-1^{BKO} mice were collected, and levels of IFNβ were determined by ELISA (n = 5 CD19$^{Cre/+}$ vs n = 6 TIM-1^{BKO} mice in e). **f**) Matrixplot depicting IFNb1 mRNA expression profile across immune populations in B16F10 tumours by scRNAseq. **g**) Tumour growth in indicated mice implanted with B16F10 melanoma and treated with isotype control or depleting anti-PDCA1 antibody (two i.p injections 48 and 24 h prior to tumour injection, n = 7 mice per group). **h**) Flow cytometry analysis of pDC (MHCII$^+$ CD11c$^+$B220$^+$PDCA1$^+$) frequencies in B16F10 CD19$^{Cre/+}$ and TIM-1^{BKO} tumours (n = 5 istoype treated and n = 3 anti-PDCA1 treated mice). Data are mean ± s.e.m and pooled from two to three independent experiments. Two-tailed Student's t-test in **b,c,e,h** and **i**. * $p < 0.05$, ** $p < 0.01$, *** $p < 0.001$, **** $p < 0.0001$, repeated measures two-way ANOVA test in **d** and **g**.

nature portfolio

Corresponding author(s): Vijay K. Kuchroo

Last updated by author(s): 2023/04/19

Reporting Summary

Nature Portfolio wishes to improve the reproducibility of the work that we publish. This form provides structure for consistency and transparency in reporting. For further information on Nature Portfolio policies, see our Editorial Policies and the Editorial Policy Checklist.

Statistics

For all statistical analyses, confirm that the following items are present in the figure legend, table legend, main text, or Methods section.

n/a	Confirmed	
☐	☒	The exact sample size (*n*) for each experimental group/condition, given as a discrete number and unit of measurement
☐	☒	A statement on whether measurements were taken from distinct samples or whether the same sample was measured repeatedly
☐	☒	The statistical test(s) used AND whether they are one- or two-sided *Only common tests should be described solely by name; describe more complex techniques in the Methods section.*
☐	☒	A description of all covariates tested
☐	☒	A description of any assumptions or corrections, such as tests of normality and adjustment for multiple comparisons
☐	☒	A full description of the statistical parameters including central tendency (e.g. means) or other basic estimates (e.g. regression coefficient) AND variation (e.g. standard deviation) or associated estimates of uncertainty (e.g. confidence intervals)
☐	☒	For null hypothesis testing, the test statistic (e.g. *F*, *t*, *r*) with confidence intervals, effect sizes, degrees of freedom and *P* value noted *Give P values as exact values whenever suitable.*
☒	☐	For Bayesian analysis, information on the choice of priors and Markov chain Monte Carlo settings
☒	☐	For hierarchical and complex designs, identification of the appropriate level for tests and full reporting of outcomes
☒	☐	Estimates of effect sizes (e.g. Cohen's *d*, Pearson's *r*), indicating how they were calculated

Our web collection on statistics for biologists contains articles on many of the points above.

Software and code

Policy information about availability of computer code

Data collection	No software was used for data collection.
Data analysis	GraphPad Prism (v9), Microsoft Excel(v15), FlowJo(v10), Cell Ranger (v3.1.0), Scanpy (v1.7.2), COMET, Scirpy (v4.2), Cumulus (v0.8), Cellbender (v0.1), Immcantation(v4.1),MiloR(v0.1), iDEP(v0.92), DESeq2 (v1.28.1)

For manuscripts utilizing custom algorithms or software that are central to the research but not yet described in published literature, software must be made available to editors and reviewers. We strongly encourage code deposition in a community repository (e.g. GitHub). See the Nature Portfolio guidelines for submitting code & software for further information.

Data

Policy information about availability of data

All manuscripts must include a data availability statement. This statement should provide the following information, where applicable:

- Accession codes, unique identifiers, or web links for publicly available datasets
- A description of any restrictions on data availability
- For clinical datasets or third party data, please ensure that the statement adheres to our policy

All genomics data produced for this study have been deposited in the NCBI Gene Expression Omnibus (GEO) under accession GSE225717.

Field-specific reporting

Please select the one below that is the best fit for your research. If you are not sure, read the appropriate sections before making your selection.

☒ Life sciences ☐ Behavioural & social sciences ☐ Ecological, evolutionary & environmental sciences

For a reference copy of the document with all sections, see nature.com/documents/nr-reporting-summary-flat.pdf

Life sciences study design

All studies must disclose on these points even when the disclosure is negative.

Sample size	Sample sizes were determined based on technical feasibility of the experimental workflow being mindful to provide a reasonable number of replicates to be confident in obtained results.
Data exclusions	As described in methods, doublets, cells with incorrect combinations of hashing antibodies or low quality (if their fraction of mitochondrial genes was ≥ 4.5% or if they had < 1,000 counts or < 300 or >6,000 genes) were discarded from the scRNAseq analysis.
Replication	Replicates were used in all experiments as noted in text, figure legends and methods. All in vivo experiments were repeated at least twice with consonant results.
Randomization	Mice were age and sex-matched and randomized where appropriate (e.g. prior to initiating treatment for matched conditions). For antibody treatments, tumors were measured and fairly distributed into groups based on size so that each group had the same approx mean growth before experimental perturbation.
Blinding	Investigators were not blinded to treatment groups or genotypes for in vivo or in vitro studies, as knowledge of this information was essential to conduct the studies. For animal studies, no blinding was performed due to requirements for cage labeling and staffing needs with the exception of replicating some tumor measurements (Fig.2, Fig.3, Fig.5) the researcher was blinded to the groupings.

Reporting for specific materials, systems and methods

We require information from authors about some types of materials, experimental systems and methods used in many studies. Here, indicate whether each material, system or method listed is relevant to your study. If you are not sure if a list item applies to your research, read the appropriate section before selecting a response.

Materials & experimental systems

n/a	Involved in the study
☐	☒ Antibodies
☐	☒ Eukaryotic cell lines
☒	☐ Palaeontology and archaeology
☐	☒ Animals and other organisms
☐	☒ Human research participants
☒	☐ Clinical data
☒	☐ Dual use research of concern

Methods

n/a	Involved in the study
☒	☐ ChIP-seq
☐	☒ Flow cytometry
☒	☐ MRI-based neuroimaging

Antibodies

Antibodies used	Surface antibodies (from Biolegend,eBioscience and BD) used in this study were diluted 1:100 and against: CD45 (30-F11,564279), TCRb (H57-597,612821), CD3e (17A2,100310), TCRbeta, CD8a (53-6.7,612898), CD4 (RM4-5,100540), CD19 (6D5,115555), B220 (RA3-6B2,564662), CD138((281-2,142506), GL-7 (GL-7,144608), Fas (Jo2, 562633), IgD (11-26c.2a, 405721), IgM (RMM-1,406506), CD21 (CR2/CR1,123422), CD43 (S7,143204), CD93 (AA4.1,136505), CD23 (B3B4,101614),TIM-1 (RMT1-4,119506), Ly6C (HK1.4,128041), Ly6G (1A8,127606), CD11c (N418,565591), CD11b (M1/70,101212), CD64 (X54-5/7.1,139316), PD-1 (RMP1-30,109112), TIGIT (1G9,142106), LAG3 (C9B7W,741350), TIM-3 (5D12,747626), CD39 (5F2,135704), CD73 (TY/11.8,127210), CD107a (1D4B,565533), NK1.1 (PK136,564144), MHC I (H-2Kb/H-2Db, 28-8-6,114605) , MHC II (I-A/E, M5/114.15.2,107645), CD80 (16-10A1,104741), CD86 (A17199A,105029), ICOSL (HK5.3,107405), CD40 (3/23,124622), CD25 (3C7,101904), IFNAR-1 (MAR1-5A3,127326). For intracellular staining: against IL-2 (JES6-5H4,503810), TNF-a (MP6-XT22,563944) and IFN-g (XMG1.2, 612769). For FOXP3 (FJK-16s,11-5773-82), Eomes (W17001A,48-4875-80), tBet (4B10,644824), Helios (22F6,137222), KI67 (16A8,652404), Granzyme B (2C5/F5,515408), Perforin (S16009A, 154310) and Tcf1 (Cell signaling C63D9,14456S). For in vivo all the antibodies were from BioXcell: anti-TIM-1 (3B3, BE0289), anti-PD-1 (RMP1-14, BE0146), anti-IFNAR-1 (MAR1-5A3, BE0241), anti-IFNGR (GR-20,BE0029), anti-PDCA1(927, BE0311)
Validation	For Tim1 most of the staining were verified using Tim-1-conditional-knockout cells. For all others FMO and isotype controls were used where appropriate. FC block was added to all stainings to reduce non-specific staining.Validation for flow antibodies was shown previously (Dixon et al. Nature 2021) Further validation is present on the manufacturer's website as noted in the Methods section.

Eukaryotic cell lines

Policy information about cell lines

Cell line source(s)	We obtained cell line; B16F10 from ATCC (CRL-6475), B16F10-Ova from Kai Wucherpfennig (Dana-Farber Cancer Institute, Boston, MA) and MC38 from Mark Smyth (QIMR Berghofer, Queensland Institute of Medical Research, Brisbane Australia). KP1.9 was derived from lung tumors of C57BL/6 KP mice and was kindly provided by Dr. A. Zippelius.
Authentication	Morphology check by microscope and growth curve analysis were performed periodically.
Mycoplasma contamination	All cell lines tested negative for mycoplasma contamination.
Commonly misidentified lines (See ICLAC register)	None of the cell lines used are listed in the ICLAC database

Animals and other organisms

Policy information about studies involving animals; ARRIVE guidelines recommended for reporting animal research

Laboratory animals	C57BL/6J, B6.129S2-Ighmtm1Cgn/J (µMT), B6.129-Prdm1tm1Clme/J (Prdm1fl/fl), Tg(CD4-cre)1Cwi (CD4Cre) and B6.129P2(C)-Cd19tm1(cre)Cgn/J (Cd19Cre), B6. Cg-Tg(TcraTcrb)425Cbn/J (OT II), B6.SJL-Ptprca Pepcb/BoyJ (CD45.1), B6.129S2-H2dlAb1-Ea/J (MHC II KO) mice were purchased from Jackson Laboratory and bred in our facility or used for experiments after at least one week of housing in our facility. CD45.1 and OT II mice were crossed to generate CD45.1-OT II mice. Havcr1fl/fl, Tigitfl/fl, Havcr2 fl/fl, Pdcd1 fl/fl, Lag3 fl/fl, Il10 fl/fl generated on C57BL/6 background and described previously (Joller et al., 2014; Xiao et al., 2015). hCD20ERT2Cre mice 82 were kindly provided by Mark Shlomchik. Floxed mice were crossed to CD4Cre, CD19Cre or hCD20ERT2Cre mice in our facility. Havcr1+/+ or Havcr1fl/fl x hCD20ERT2Cre (hCD20TamCre and TIM-1iBKO) mice were gavaged with 4mg Tamoxifen in 200µl corn oil on days indicated in the figure. While TIM-1fl/fl and CD19Cre/+ animals had a similar tumor growth profile (not shown), we preferentially used the CD19Cre/+ mice as controls since this strain has been generated as “knock-in/knock-out” which partially impairs CD19 expression. Braf-Pten mice (B6.Cg-Braftm1Mmcm Ptentm1Hwu Tg(Tyr-cre/ERT2)13Bos/BosJ), and ZsG mice (B6.Cg-Gt(ROSA)26Sortm6(CAG-ZsGreen1)Hze/J) were purchased from The Jackson Laboratory. Female mice at the age of 4–10 weeks were used for experiments. Housing - Innovive® individually ventilated cages. Food - ad libitum, Teklad® Global 18% Protein Rodent Diet, irradiated. Water - Sterile prefilled bottles. Dark/Light cycle on a 12 hour automated schedule. Temperature ambient and humidity within parameters of IACUC guidelines 30-70%.
Wild animals	No Wild animals were used in this study
Field-collected samples	no field collected samples were used in the study.
Ethics oversight	All experiments were conducted in accordance with animal protocols approved by the Harvard Medical Area Standing Committee on Animals or BWH and MGH IACUC.

Note that full information on the approval of the study protocol must also be provided in the manuscript.

Human research participants

Policy information about studies involving human research participants

Population characteristics	4 healthy individuals, age 24-35, 3/1 (f/m)
Recruitment	from lab staff
Ethics oversight	Ethics approval from the local ethics committee of the Medical University of Graz (29-586ex16-17)

Note that full information on the approval of the study protocol must also be provided in the manuscript.

Flow Cytometry

Plots

Confirm that:

☒ The axis labels state the marker and fluorochrome used (e.g. CD4-FITC).

☒ The axis scales are clearly visible. Include numbers along axes only for bottom left plot of group (a 'group' is an analysis of identical markers).

☒ All plots are contour plots with outliers or pseudocolor plots.

☒ A numerical value for number of cells or percentage (with statistics) is provided.

Methodology

Sample preparation	For single cell suspension: lymph nodes and spleens were mechanically dissociated, homogenized, and passed through a 40-

Sample preparation	µm cell strainer and lysed of red blood cells (RBCs; using ACK buffer) then washed with cold PBS and spun down. Tumors were dissociated mechanically and digested with 1 mg/mL collagenase A and 0.1 mg/mL DNase1 for 20 min at 37°C. Live/dead cell discrimination was performed using Live/Dead Fixable viability dye e506 (eBioscience).
Instrument	BD Symphony A5 (BD Biosciences) and BD FACSAria™ for cell sorting
Software	FlowJo (Tree Star).
Cell population abundance	The frequency of the purity for the populations of interest are specified in the appropriate figures/methods.
Gating strategy	Cells were first gated for FSC/SSC, doublets were excluded based on FSC and SSC W/H parameters, then onlive CD45+ followed by population specific markers.

☒ Tick this box to confirm that a figure exemplifying the gating strategy is provided in the Supplementary Information.